

1 **Supplementary Materials**

2 **AI-boosted and motion-corrected, wireless near-infrared sensing system for continuously**
3 **monitoring laryngeal muscles**

4 Yihan Liu, Arjun Putcha, Gavin Lyda, Nanqi Peng, Salil Pai, Tien Nguyen, Sicheng Xing, Shang Peng,
5 Yiyang Fan, Yizhang Wu, Wanrong Xie, Wubin Bai

6 Corresponding author: Wubin Bai, wbai@unc.edu

7 **The PDF file includes:**

8 Note S1 to S6

9 Table S1 to S5

10 Figure S1 to S47

11 Movie captions S1 to S2

12 References

13 **Other Supplementary Material for this manuscript includes the following:**

14 Movies S1 to S2

15

1 **Note S1. Theory and implementation of Madgwick filter**

2 The Madgwick filter combines data from accelerometers, gyroscopes, and, optionally, magnetometers
 3 to estimate three-dimensional orientation with high precision¹. Generally, the orientation of a rigid body
 4 or coordinate frame can be represented by a quaternion, which is a four-dimensional complex number.
 5 For example, if the one arbitrary axis of frame A is represented by the unit vector ${}^A\hat{\mathbf{r}} = [r_x \ r_y \ r_z]$, then
 6 the orientation of frame B relative to frame A is represented by the following quaternion.

7
$${}^B\hat{\mathbf{q}} = [q_1 \ q_2 \ q_3 \ q_4] = \left[\cos \frac{\theta}{2} \ - r_x \sin \frac{\theta}{2} \ - r_y \sin \frac{\theta}{2} \ - r_z \sin \frac{\theta}{2} \right] \quad (1)$$

8 In equation (1), the rotation angle θ is defined from the angle between frames A and B when they are
 9 aligned by the axis ${}^A\hat{\mathbf{r}}$. With this definition, two more basic quaternion calculations with physical
 10 significance can be defined. The conjugate of the quaternion ${}^B\hat{\mathbf{q}}$, is the one that describes the relative
 11 orientation of frame A to frame B.

12
$${}^B\hat{\mathbf{q}}^* = {}^A\hat{\mathbf{q}} = [q_1 \ - q_2 \ q_3 \ - q_4] \quad (2)$$

13 The outer product determines the compound orientation.

14
$${}^C\hat{\mathbf{q}} = {}^B\hat{\mathbf{q}} \otimes {}^A\hat{\mathbf{q}} \quad (3)$$

15
$$a \otimes b = [a_1 \ a_2 \ a_3 \ a_4] \otimes [b_1 \ b_2 \ b_3 \ b_4] = \begin{bmatrix} a_1b_1 - a_2b_2 - a_3b_3 - a_4b_4 \\ a_1b_2 + a_2b_1 + a_3b_4 - a_4b_3 \\ a_1b_3 - a_2b_4 + a_3b_1 + a_4b_2 \\ a_1b_4 + a_2b_3 - a_3b_2 + a_4b_1 \end{bmatrix}^T \quad (4)$$

16 With that, we can write the coordinates translation for a vector \mathbf{v} changing from frame A to frame B.
 17 Here, ${}^A\mathbf{v}$ and ${}^B\mathbf{v}$ are the coordinates of the same vector \mathbf{v} under frame A and frame B, respectively.

18
$${}^B\mathbf{v} = {}^B\hat{\mathbf{q}} \otimes {}^A\mathbf{v} \otimes {}^A\hat{\mathbf{q}} \quad (5)$$

19 This can also be described by a rotation ${}^B\mathbf{R}$ that applies to the vector ${}^A\mathbf{v}$.

20
$${}^B\mathbf{R} = \begin{bmatrix} 2q_1^2 - 1 + 2q_2^2 & 2(q_2q_3 + q_1q_4) & 2(q_2q_4 - q_1q_3) \\ 2(q_2q_3 - q_1q_4) & 2q_1^2 - 1 + 2q_3^2 & 2(q_3q_4 + q_1q_2) \\ 2(q_2q_4 + q_1q_3) & 2(q_3q_4 - q_1q_2) & 2q_1^2 - 1 + 2q_4^2 \end{bmatrix} \quad (6)$$

21 The same rotation can be achieved by performing a sequence of rotations from the alignment with
 22 frame A on frame B. These rotations are defined by the following equation.

23
$$\begin{bmatrix} \psi \\ \theta \\ \varphi \end{bmatrix} = \begin{bmatrix} \text{atan2}(2q_2q_3 - 2q_1q_4, 2q_1^2 + 2q_2^2 - 1) \\ -\sin^{-1}(2q_2q_4 + 2q_1q_3) \\ \text{atan2}(2q_3q_4 - 2q_1q_2, 2q_1^2 + 2q_4^2 - 1) \end{bmatrix} \quad (7)$$

24 In equation (7), the function atan2 is the 2-argument arctangent that measures the phase angle of a
 25 complex number $x + iy$. Euler angles ψ, θ, φ are the rotation angles around $\hat{\mathbf{z}}_B, \hat{\mathbf{y}}_B, \hat{\mathbf{x}}_B$, respectively.

1 In a realistic scenario where an IMU is measuring the angular speed and acceleration of itself in the
 2 earth frame, we have the following results:

$$3 \quad {}_E^S \dot{\mathbf{q}}_{\omega,t} = \frac{1}{2} {}_E^S \hat{\mathbf{q}}_{est,t-1} \otimes {}^S \boldsymbol{\omega}_t \quad (8)$$

$$4 \quad {}_E^S \mathbf{q}_{\omega,t} = {}_E^S \hat{\mathbf{q}}_{est,t-1} + {}_E^S \dot{\mathbf{q}}_{\omega,t} \Delta t \quad (9)$$

$$5 \quad f({}_E^S \hat{\mathbf{q}}, {}^E \hat{\mathbf{d}}, {}^S \hat{\mathbf{s}}) = {}_E^S \hat{\mathbf{q}}^* \otimes {}^E \hat{\mathbf{d}} \otimes {}_E^S \hat{\mathbf{q}} - {}^S \hat{\mathbf{s}} \quad (10)$$

$$6 \quad {}_E^S \mathbf{q}_{\nabla,t} = {}_E^S \hat{\mathbf{q}}_{est,t-1} - \mu_t \frac{\nabla f}{\| \nabla f \|} \quad (11)$$

$$7 \quad \nabla f = J_g^T({}_E^S \hat{\mathbf{q}}_{est,t-1}) f_g({}_E^S \hat{\mathbf{q}}_{est,t-1}, {}^S \hat{\mathbf{a}}_t) \quad (12)$$

8 In equation (8), S and E represent the sensor frame and the earth frame, respectively. ${}^S \boldsymbol{\omega}_t$ is the
 9 angular rate vector $[0 \ \omega_x \ \omega_y \ \omega_z]$ measured by the gyroscope, ${}_E^S \dot{\mathbf{q}}_{\omega,t}$ is the relative orientation changing
 10 rate of the earth frame relative to the sensor frame at the time t . With equation (5), the calculated
 11 quaternion at time t , ${}_E^S \mathbf{q}_{\omega,t}$, can be derived from the estimated quaternion of the earth frame at time $(t -$
 12 $1)$, the orientation changing rate at time t , and the sampling interval of the sensor Δt (equation (9)).
 13 However, with just the observation from the gyroscope, the estimation of the quaternion will not yield a
 14 unique solution due to the unknown direction of the earth's gravity field in the earth frame. This will
 15 eventually leave the orientation perpendicular to the gravity field undecided. A complete and unique
 16 solution can be found by solving the optimization problem of minimizing the objective function f , whose
 17 definition can be found in equation (10). In this function, ${}^E \hat{\mathbf{d}}$ is a reference vector of the earth frame
 18 and ${}^S \hat{\mathbf{s}}$ is the measured direction in the sensor frame. Solving the optimization problem leads to
 19 equation (11), where $\mu_t = \alpha \| {}_E^S \dot{\mathbf{q}}_{\omega,t} \| \Delta t$ ($\alpha > 1$, is a noise cancellation factor) is the step-size in the
 20 optimization, ∇f is the gradient of the solution surface, defined by its Jacobian and the optimization
 21 function, calculated in equation (12). Note that in equation (12), the general form ${}^E \hat{\mathbf{d}}$ and ${}^S \hat{\mathbf{s}}$ have been
 22 replaced by the measurables, ${}^E \hat{\mathbf{g}} = [0 \ 0 \ 0 \ 1]$, (gravity) and ${}^S \hat{\mathbf{a}} = [0 \ a_x \ a_y \ a_z]$ (accelerations).

23 Combining the estimation from equation (8) and equation (11) will lead to the Madgwick filter fusion
 24 algorithm.

$$25 \quad {}_E^S \mathbf{q}_{est,t} = \gamma_t {}_E^S \mathbf{q}_{\nabla,t} + (1 - \gamma_t) {}_E^S \mathbf{q}_{\omega,t}, \quad 0 < \gamma_t < 1 \quad (13)$$

26 This equation can be simplified by optimizing the choice of γ_t . Eventually we will have the following
 27 form.

$$28 \quad {}_E^S \mathbf{q}_{est,t} = {}_E^S \hat{\mathbf{q}}_{est,t-1} + {}_E^S \dot{\mathbf{q}}_{est,t} \Delta t \quad (14)$$

$$29 \quad {}_E^S \dot{\mathbf{q}}_{est,t} = {}_E^S \dot{\mathbf{q}}_{\omega,t} - \beta {}_E^S \dot{\mathbf{q}}_{\epsilon,t} \quad (15)$$

$$30 \quad {}_E^S \dot{\mathbf{q}}_{\epsilon,t} = \frac{\nabla f}{\| \nabla f \|} \quad (16)$$

1 Here, β is the divergence rate of ${}^S_E\dot{\mathbf{q}}_\omega$ expressed as the magnitude of the quaternion derivative with
 2 respect to the gyroscope measurement error, and ${}^S_E\dot{\mathbf{q}}_{\epsilon,t}$ is the direction of the estimated error. With
 3 equations (14) to (16), we can calculate the quaternion ${}^S_E\mathbf{q}_{est,t}$ at a given time t and filter out the error
 4 item $\beta {}^S_E\dot{\mathbf{q}}_{\epsilon,t}$ in the measurements of gyroscope and accelerometer. In this project, our selection of Δt is
 5 based on the sample rate of the IMU, which is 0.001 s. The Madgwick filter is implemented on the MCU
 6 to avoid the error caused by the data transmission delay.

7

8 **Note S2. Monte Carlo simulation setup for device validation and data visualization.**

9 **Monte Carlo simulation implementation.** Monte Carlo (MC) methods have been widely used in
 10 statistical computing in complex systems². Specifically, in an optical simulation in a biological tissue, a
 11 large group of photons are launched into the test area, namely, a voxel space, and can migrate in the
 12 voxel space under the boundary condition regarding each voxel. In this project, we used a time-stepped
 13 simulation to show the maximum scatter profile in a short period (nanosecond-level) after the launching
 14 of the photons, given the assumption that the photons shot from the light source are continuous. The
 15 main consideration of the voxel boundary conditions includes reflection, scattering, and attenuation. (1)
 16 Reflection. This calculation is based on the reflection coefficient of the current medium. According to
 17 Fresnel's equation, the photon wave packet vector is mirrored when a different medium is detected at
 18 the next voxel along the vector. (2) Scattering. This behavior is determined by the scattering coefficient
 19 of the current medium. A scattering length and scattering direction vector are calculated before the
 20 scattering event and is implemented after the event is committed by comparing the traveled distance
 21 from the last event and the scattering length. (3) Attenuation. This behavior is determined by the
 22 absorption coefficient of the current medium. For every time step of the simulation, the photon packet
 23 weight is reduced by this coefficient.

24 **System setup considerations.** In the configuration of the MC optical simulation in human tissue, the
 25 most important factors are light source setup and voxel space construction.

26 (1) Light source. The light source needs to be fine-tuned in a MC setup to guide the initial orientations
 27 of the photon wave packet vectors. Most wearable NIRS devices use an NIR LED as their light sources
 28 who has a spatial light intensity distribution known as the Lambertian distribution.

$$29 \quad I(\theta) = I_0 \cos \theta = I_0 \cos \left[\tan^{-1} \left(\sqrt{x^2 + y^2} \right) \right] \quad (17)$$

30 Here, θ denotes the angle between the irradiance and the normal axis of the light source. In real
 31 scenarios, to accelerate the computation of photon trajectories, it is possible to use an angular
 32 Gaussian distribution to approximate the LED intensity distribution (**Figure S43**).

$$33 \quad I(\theta) = I_0 e^{-\frac{1}{2}\left(\frac{\theta}{\sigma}\right)^2} = I_0 e^{-\frac{(x-\mu_x)^2}{2\sigma_x^2} - \frac{(y-\mu_y)^2}{2\sigma_y^2}} \quad (18)$$

34 In equation (18), σ denotes the variance in the zenith angle of an initial photon wave packet vector
 35 launched from the light source. **Figure S43** shows an example of the comparison between the angular
 36 Gaussian distribution and Lambertian distribution, confirming the feasibility of this approximation.

1 (2) Voxel space construction. According to the above, the MC simulation requires a pre-defined
2 behavior at every voxel boundary. Thus, this step requires setting the scattering coefficient μ_s , the
3 absorption coefficient μ_a , and the refractive index n of every voxel.

4 **Parameters used in the MC simulation.** Demonstrated in Table S4^{3–5}.

5 **Simulation performance.** Within the normal status (NS) portion, the skin geometry was initialized as a
6 voxel space containing a set of parallel layers: the epidermis, dermis, subcutaneous adipose, and
7 muscle, whose thicknesses were found to be 1.5 mm, 3.5 mm, 10 mm, and 35 mm, respectively. The
8 simulation itself was configured by establishing the seed (i.e., the starting point for random number
9 generation), the number of photons used, and the level of debug output of the MC simulation. The
10 configurations were then used to define the light detector and source: the near-infrared photon packets
11 emitted from the source would reflect perpendicularly, following an angular Gaussian distribution to
12 approximate the LED intensity distribution. After configuring the plots in which the results would be
13 graphed, this information was used by the bump translate (BP) portion for data visualization. In a set
14 60-by-10 array, several inputs were established for the tracking and representation of the movement of
15 the LP over the course of the physiological activities identified for the experiment. The simulation began
16 at the timepoint designated as 0, with the time step and end respectively defined as 1 and 500
17 picoseconds. The voxel space is modified from the parallel pattern used in the first simulation. Here, a
18 2D Gaussian function (GF) on the layer boundary is used to approximate the shape of the LP. The
19 mean value of the GF defines the vertical location of the LP's peak. The amplitude of the GF defines
20 the horizontal location of the LP's peak relative to the surface of the skin. The variance of the GF
21 defines the size of the LP. In addition to those, the tissue thicknesses, offset, and box size, are utilized
22 to generate the Gaussian approximation of the LP. This generation was looped 600 times over the
23 simulation—with one run per 0.5 nanoseconds—recording the fluence at every voxel at the end of each
24 run, the movement of the LP, and the trajectory and weight loss of each emitted near-infrared photon
25 packet as it traveled along its path (**Fig. 5B-C**).

27 Note S3. Device firmware operating principle

28 **Sensor Initialization.** The four-channel ADC (ADS1115) is initialized with the following settings:
29 measurement mode - continue; gain level - 4.096V; data rate - 860 samples per second. This setup will
30 enable continuous reading from four PDs. The IMU sensor is initialized with the following settings:
31 accelerator measure scale - $\pm 2g$; gyroscope measure scale - 250 degrees per second; output data rate
32 (ODR) - 1000 Hz. These parameters are tailored to capture high-precision movement data. The
33 Madgwick filter is employed with the IMU, providing a real-time approximation of the device's
34 orientation in space (Euler angles: yaw, pitch, and roll). The sampling rate of the Madgwick filter is set
35 to 1000 Hz, which is the same sampling rate as the IMU.

36 **Data Acquisition and Processing.** Since the ambient environment can be unpredictable, wireless
37 data transmission can sometimes jam the on-board data acquisition. To resolve this, the system utilizes
38 a hardware timer to manage data acquisition intervals, ensuring consistent sampling rates for accurate
39 signal processing, independent of the data transmission speed. The hardware timer is set to send a
40 trigger every millisecond. The trigger signal enables one data update at all seven channels. In one
41 iteration, the MCU first measures the current time from the device boot. The IMU data then sends the
42 six measurements to the Madgwick filter, which updates the real-time Euler angles. Finally, the ADC
43 accesses the photovoltages from four PDs in the following sequence: central, bottom, top left, and top

1 right. The data is compiled into a comma-separated string to minimize the size of the whole data
2 package.

3 **Wireless Communication and user-interactivity.** BLE technology facilitates real-time data
4 transmission to a connected client, such as another MCU, a smartphone, or a PC. The system
5 dynamically adjusts its operation based on the connection status, ensuring data are broadcast when a
6 client is connected and conserving resources when in standby. Additionally, BLE connection callbacks
7 manage the system's advertising state, ensuring it remains discoverable by potential clients after
8 disconnected. A real-time, multiprocessing Bluetooth app, BTviz, is used to read, preprocess, and
9 visualize data. (**Figure S45**) The user will first press the “Scan for Devices” button for the app to scan
10 for all advertising Bluetooth devices in the environment. Then, the user will select the “LaHMo” sensor
11 from the list and select connect to device. From there, the user will select the corresponding service
12 and characteristics from the list to read using “Read Service” button and double click at the
13 characteristic. Finally, BTviz will show the real-time plotting of the selected measurement.

14

15 **Note S4. Data preprocessing principle**

16 **Butterworth filter.** Butterworth filter is an infinite impulse response (IIR) filter with a transfer function
17 $H(s) = \frac{1}{1 + \left(\frac{s}{\omega_c}\right)^{2N}}$, where $H(s)$ is the transfer function in the complex frequency domain (s-plane), ω_c is
18 the cutoff frequency (in radians per second), and N is the order of the filter. To implement the
19 Butterworth filter in a digital system, the transfer function needs to be converted from the continuous-
20 time domain (s-plane) to the discrete-time domain (z-plane). This is done using the bilinear
21 transformation, which maps the left half of the s-plane to the inside of the unit circle in the z-plane.

$$22 \quad s = \frac{2}{T} \left(\frac{z - 1}{z + 1} \right) \quad (19)$$

23 Here, T is the sampling period. Applying the bilinear transformation to the Butterworth transfer function
24 yields the discrete-time transfer function.

$$25 \quad H(z) = \frac{b_0 + b_1 z^{-1} + \dots + b_M z^{-M}}{1 + a_1 z^{-1} + \dots + a_N z^{-N}} \quad (20)$$

26 Here, b_i are the numerator coefficients, a_i are the denominator coefficients, M and N are the order of
27 the numerator and denominator polynomials. After this, the filter transfer function is further factored into
28 a series of second-order sections (SOS), each with its own numerator and denominator coefficients.
29 This transfer function of SOS is given by:

$$30 \quad H_i(z) = \frac{b_{i0} + b_{i1} z^{-1} + b_{i2} z^{-2}}{1 + a_{i1} z^{-1} + a_{i2} z^{-2}} \quad (21)$$

31 where b_{i0} , b_{i1} , b_{i2} are the numerator coefficients of the i-th SOS, and a_{i1} , a_{i2} are the denominator
32 coefficients of the i-th SOS. With this, the overall transfer function of the filter can be written as $H(z) =$
33 $H_1(z) \cdot H_2(z) \cdot \dots \cdot H_n(z)$, where n is the number of SOSs.

1 After the SOS arrays are obtained, the input signal is first padded on both ends to minimize startup and
2 ending transients. Then the SOS filters are applied to the input signal in the forward direction using the
3 difference equation $y[n] = b_{i0}x[n] + b_{i1}x[n - 1] + b_{i2}x[n - 2] - a_{i1}y[n - 1] - a_{i2}y[n - 2]$, where $x[n]$ is
4 the input signal at the time step n , and $y[n]$ is the output signal at time step n . With that, all the SOS
5 arrays are reversed before reapplied to the previously filtered signal. The padded length is trimmed to
6 recover the initial signal length before the final output.

7 **Peak locating.** The implementation of peak locating is based on the `find_peaks()` function from the
8 SciPy library. The algorithm used by `find_peaks()` can be separated into several parts. First, the
9 difference between adjacent elements in the input array x is calculated to form a new array dx . Second,
10 in the array dx , the point where it changes from positive to negative is located. The found point(s)
11 indicate a critical point of the original array x . Specifically, `find_peaks()` allows additional criteria, and
12 the one used in this protocol is the distance, namely, the minimum distance by which peaks are
13 considered. If one peak is detected within the minimum distance from the last peak, it will not be
14 counted.

15 **Peak expansion.** This step gives a window of specified size n for final classification. The algorithm first
16 picks the peaks from the previous step, then for each peak, the algorithm creates an empty window of
17 size n before filling it with data from original signal starting from $p - \left\lceil \frac{n}{2} \right\rceil$ to $p + \left\lceil \frac{n}{2} \right\rceil$, where p is the index
18 of the peak. Repeating this process will eventually result in an expanded array with a dimension (N_p, n) ,
19 where N_p is the number of peaks.

20 **Note S5. Reduction of motion artifact with LaHMo patch and dual-GRU model**

21 The LaHMo platform integrates two key strategies to reduce the motion artifact that is ubiquitous in
22 NIRS measurements: i) the use of an IMU to capture motion signals and ii) the application of the dual-
23 GRU model to analyze and differentiate the signals from both the IMU and NIRS modalities. The IMU is
24 incorporated into the LaHMo platform to detect and measure motion signals, which is a common
25 technique used to calibrate NIRS signals. The IMU provides real-time data on the subject's movement,
26 represented as a time series $\mathbf{M}(t)$ where t denotes time. This data helps identify and account for
27 motion artifacts that might otherwise be misinterpreted as physiological signals in the NIRS data $\mathbf{N}(t)$.
28 By capturing $\mathbf{M}(t)$, the IMU allows us to correlate motion data with NIRS data and effectively filter out
29 components of $\mathbf{N}(t)$ that are caused by motion rather than true physiological activity. To demonstrate
30 how the dual-GRU model processes both the IMU and NIRS data to isolate physiological signals from
31 motion artifacts, we can examine the mechanism of the dual-GRU architecture. First, the hidden state
32 of NIRS, $\mathbf{h}_N(t)$ can be given by the following expressions:

$$33 \quad \mathbf{h}_N(t) = (1 - \mathbf{z}_N(t)) \circ \mathbf{h}_N(t - 1) + \mathbf{z}_N(t) \circ \tilde{\mathbf{h}}_N(t)$$

$$34 \quad \tilde{\mathbf{h}}_N(t) = \tanh(\mathbf{W}_{hN}\mathbf{N}(t) + \mathbf{r}_N(t) \circ (\mathbf{U}_{hN}\mathbf{h}_N(t - 1)) + \mathbf{b}_h)$$

35 where $\mathbf{z}_N(t)$ and $\mathbf{r}_N(t)$ are the update and reset gates, \mathbf{W}_{hN} and \mathbf{U}_{hN} are weight matrices, and \mathbf{b}_h is the
36 bias term. \circ denotes the Hadamard (element-wise) product. The same applies to the hidden state of
37 IMU modality, $\mathbf{h}_M(t)$. After the two hidden states are acquired, the two hidden states are then
38 concatenated to form a combined hidden state before passed through an output layer:

$$1 \quad \mathbf{h}_c(t) = \begin{bmatrix} \mathbf{h}_N(t) \\ \mathbf{h}_M(t) \end{bmatrix}$$

$$2 \quad \mathbf{y}(t) = \sigma(\mathbf{W}_o \cdot \mathbf{h}_c(t) + \mathbf{b}_o)$$

3 Here, \mathbf{W}_o and \mathbf{b}_o are the weight matrix and the bias term of the dense layer, respectively. σ is the
 4 rectified linear unit (ReLU) activation function. The output $\mathbf{y}(t)$ represents the filtered physiological
 5 signal. This layer allows the model to effectively exclude the influence of the motion by assigning
 6 different weight for each signal in each modality, ensuring that $\mathbf{y}(t)$ primarily reflects true physiological
 7 activities.

8 **Note S6 Domain adaptation for system individualization.**

9 Training neural networks can be time-consuming and inconvenient for users. A large neural network,
 10 while highly capable, would be limited to a single user, requiring every target user to undertake an
 11 extensive training procedure. The main training process demonstrated in the right portion of **Fig. S34A**
 12 uses 99 samples from the sample subject. Having the same number of samples to train the model every
 13 time a target user is introduced can bring significant inconvenience and substantial cost of time and
 14 resources. To make the platform easily accessible and adaptable to a broad range of users, the network
 15 must be small and localized, capable of harnessing a larger remote network while remaining customized
 16 to each individual. Domain adaptation is a technique in machine learning that allows a model trained on
 17 one domain (source domain) to be applied to another domain (target domain) by leveraging the
 18 knowledge learned from the source domain. This approach is particularly useful when the target domain
 19 has limited labeled data, as it enables the model to learn from the abundant data in the source domain
 20 and adapt to the target domain with minimal additional training. In the context of the LaHMo platform, we
 21 introduce an adapted version of the dual-GRU model, adaptive-GRU (adap-GRU), which utilizes domain
 22 adaptation to facilitate individualization of the AI analysis. The adap-GRU model is designed to be a
 23 lightweight adaptation network that can be quickly trained on a small dataset from a target user while
 24 leveraging the knowledge gained from a pre-trained dual-GRU model on a comprehensive dataset from
 25 a sample subject. The domain adaptation strategy shows two significant advantages over its pre-trained
 26 base: 1) a significantly smaller size that requires less time to train, and 2) high personalization where
 27 users can customize the selection of available actions for a model tailored for individual needs (e.g.
 28 speech, swallow, or others) (40, 41).

29 As shown in **Fig. S34A**, a small adaptation network, based on the adapted dual-GRU (adap-GRU),
 30 employs a series of fast executable additional layers, as an adaptation model, which is preceded by the
 31 core neural network architecture previously trained on a comprehensive dataset, a dual-GRU, that serves
 32 as the base model. The adap-GRU network incorporates an adaptation network that comprises two linear
 33 transformation layers for each input channel, augmented by rectified linear unit (ReLU) activations,
 34 effectively projecting the input data into a space amenable to the domain of the original model without
 35 necessitating extensive retraining. Compared with training a dual-GRU, the training for adap-GRU also
 36 requires fewer types of samples requiring only four datasets from the user to be fed to a generalized, pre-
 37 trained dual-GRU. **Fig. S35B** shows the data from the target user different from the source user shown
 38 in **Fig. 2E**, thus exhibiting hat significant difference in their signal characteristics. This is an expected
 39 behavior due to the natural variations between individual characteristics. Data from four physiological
 40 activities, dry cough, swallowing, throat clearing, and aerobic workout, is necessary for this training
 41 process. The predicted result of adap-GRU is shown in **Fig. S35**.

1 To validate the efficacy of this approach, we compared the training curve of the adap-GRU and dual-GRU
2 (**Fig. S34C**). The results show that adap-GRU is trained much faster with a pre-trained dual-GRU (red
3 curve), compared to the training process of starting a new dual-GRU network. The ES point can be
4 chosen to be epoch = 30, where the training dataset reaches an accuracy of 90.3% and the testing
5 dataset reaches an accuracy of 85.7%, whereas the accuracies at this stage for dual-GRU are less, the
6 training dataset at 65.4% and the testing dataset at 42.9%. Upon completion of the training, the adap-
7 GRU was tested, predicting physiological events executed by an unknown user (**Fig. S35**). The
8 subsequent confusion matrix of the four training activities shows a similar performance to that of the dual-
9 GRU trained on the sample subject, confirming the effectiveness of adap-GRU on target user system
10 individualization (**Fig. S34D**). The accuracy of adap-GRU in incident classification was 0.81 for dry
11 coughing, 1.00 for swallowing, 0.90 for throat clearing, and 0.90 for aerobic exercising, with the
12 physiological events respectively represented by the labels 1, 2, 4, and 5. Since it yields a similar
13 performance of the adap-GRU to the source user-trained dual-GRU, with fewer data inputs and fewer
14 training epochs, it can be concluded that this method enables facile adaptability to be inclusive in both
15 user adoption and activity categorization.

1 **Table S1. Bill of materials for LaHMo patch**

Name	Designator	Quantity	Manufacturer
2450AT18B100E	ANT1	1	Johanson
GRM0335C1E120JA01D	C1, C2, C3, C4, C5, C6, C10, C11, C19, C20	10	Murata
GRM32DR71E106KA12L	C7	1	Murata
GCM188D71H105KE36J	C8, C9, C12, C13, C14, C17, C18	7	Murata
C0402C309B5GACTU	C15, C16	2	Yageo
SFH_4043	D1, D2, D3, D4	4	Osram
ESP32-C3FH4	IC1	1	Espressif
LQP03HQ2N0W02D	L1	1	Murata
LQW15AN2N4G80D	L2	1	Murata
VEMD1060X01	PD1, PD2, PD3, PD4	4	Vishay Semiconductors
RC0201FR-071ML	R1, R2, R3, R4	4	Yageo
ERA-1AEB103C	R5, R8, R9, R10, R15	5	Panasonic
CR0402-JW-202GLF	R6, R7, R11, R12	4	Bourns
CR0402-JW-102GLF	R13, R14, R16	3	Bourns
TLV9002IDSGT	U1, U2	2	Texas Instruments
LSM6DSOXTR	U3	1	STMicroelectronics
MIC94041YFLTR	U4, U5, U6, U7	4	Microchip
ADS1115IRUGT	U8	1	Texas Instruments
ADP7118ACPZN3.3-R7	U9	1	Analog Devices
vABM11W-40.0000MHZ-8-B1U-T3	Y1	1	Abraccon
ABS07-32.768KHZ-9-T	Y2	1	Abraccon

2

3

1 **Table S2 Detailed information of the activity(ies) each participant performed***

# participant	# activity
1	(1)
2	(1), (2), (3)
3	(4)

2 * Activity (1): A short test lasts for 6 minutes. The participant performs the following activities for 1
3 minute each: deep breathing, dry cough, swallowing, throat clearing, running in place, and push-ups.
4 The participant will perform each activity at his or her own pace for 1 minute. Activity (2): An extended
5 short test lasts for 8 minutes. The participant performs the following activities for 30 seconds each:
6 sitting still, deep breathing, throat clearing, swallowing, yawning, dry cough, randomly talking, sneezing,
7 cervical flexion, cervical extension, cervical rotation, cervical side-bending, sit down and stand up,
8 walking in place, jumping, and biking. Activity (3): A repeating test lasts for 1 – 2 minutes, the participant
9 repeats one of the following activities: dry cough, swallowing, or pronouncing a specific phoneme.
10 Activity (4): An exercise test lasts for 1 hour. The participant performs the following activities on a
11 basketball court with a basketball: dribbling around the court, switchback run, shooting, and layups.

1 **Table S3 List of the layer composition and dimensions of all tested networks**

Network type	Layer name	Type (Dimension)
PV-biased FRNN	FRNN	torch.nn.RNN (4, 140)
	FC	torch.nn.Linear (140, 6)
	SM	torch.nn.LogSoftmax (6, 1)
PV-biased BiFRNN	FRNN	torch.nn.RNN (4, 280)
	FC	torch.nn.Linear (280, 6)
	SM	torch.nn.LogSoftmax (6, 1)
PV-biased LSTM	LSTM	torch.nn.LSTM (4, 140)
	FC	torch.nn.Linear (140, 6)
	SM	torch.nn.LogSoftmax (6, 1)
PV-biased BiLSTM	LSTM	torch.nn.LSTM (4, 280)
	FC	torch.nn.Linear (280, 6)
	SM	torch.nn.LogSoftmax (6, 1)
PV-biased GRU	GRU	torch.nn.GRU (4, 140)
	FC	torch.nn.Linear (140, 6)
	SM	torch.nn.LogSoftmax (6, 1)
PV-biased BiGRU	GRU	torch.nn.GRU (4, 280)
	FC	torch.nn.Linear (280, 6)
	SM	torch.nn.LogSoftmax (6, 1)

2

3

Network type	Layer name	Type (Dimension)
IMU-biased FRNN	FRNN	torch.nn.RNN (3, 140)
	FC	torch.nn.Linear (140, 6)
	SM	torch.nn.LogSoftmax (6, 1)
IMU-biased BiFRNN	FRNN	torch.nn.RNN (3, 280)
	FC	torch.nn.Linear (280, 6)
	SM	torch.nn.LogSoftmax (6, 1)
IMU-biased LSTM	LSTM	torch.nn.LSTM (3, 140)
	FC	torch.nn.Linear (140, 6)
	SM	torch.nn.LogSoftmax (6, 1)
IMU-biased BiLSTM	LSTM	torch.nn.LSTM (3, 280)
	FC	torch.nn.Linear (280, 6)
	SM	torch.nn.LogSoftmax (6, 1)
IMU-biased GRU	GRU	torch.nn.GRU (3, 140)
	FC	torch.nn.Linear (140, 6)
	SM	torch.nn.LogSoftmax (6, 1)
IMU-biased BiGRU	GRU	torch.nn.GRU (3, 280)
	FC	torch.nn.Linear (280, 6)
	SM	torch.nn.LogSoftmax (6, 1)

1

2

Network type	Layer name	Type (Dimension)
IMU-biased FRNN	FRNN	torch.nn.RNN (3, 140)
	FC	torch.nn.Linear (140, 6)
	SM	torch.nn.LogSoftmax (6, 1)
IMU-biased BiFRNN	FRNN	torch.nn.RNN (3, 280)
	FC	torch.nn.Linear (280, 6)
	SM	torch.nn.LogSoftmax (6, 1)
IMU-biased LSTM	LSTM	torch.nn.LSTM (3, 140)
	FC	torch.nn.Linear (140, 6)
	SM	torch.nn.LogSoftmax (6, 1)
IMU-biased BiLSTM	LSTM	torch.nn.LSTM (3, 280)
	FC	torch.nn.Linear (280, 6)
	SM	torch.nn.LogSoftmax (6, 1)
IMU-biased GRU	GRU	torch.nn.GRU (3, 140)
	FC	torch.nn.Linear (140, 6)
	SM	torch.nn.LogSoftmax (6, 1)
IMU-biased BiGRU	GRU	torch.nn.GRU (3, 280)
	FC	torch.nn.Linear (280, 6)
	SM	torch.nn.LogSoftmax (6, 1)

1

2

Network type	Layer name	Type (Dimension)
mono-FRNN	FRNN	torch.nn.RNN (7, 140)
	FC	torch.nn.Linear (140, 6)
	SM	torch.nn.LogSoftmax (6, 1)
mono-BiFRNN	FRNN	torch.nn.RNN (7, 280)
	FC	torch.nn.Linear (280, 6)
	SM	torch.nn.LogSoftmax (6, 1)
mono-LSTM	LSTM	torch.nn.LSTM (7, 140)
	FC	torch.nn.Linear (140, 6)
	SM	torch.nn.LogSoftmax (6, 1)
mono-BiLSTM	LSTM	torch.nn.LSTM (7, 280)
	FC	torch.nn.Linear (280, 6)
	SM	torch.nn.LogSoftmax (6, 1)
mono-GRU	GRU	torch.nn.GRU (7, 140)
	FC	torch.nn.Linear (140, 6)
	SM	torch.nn.LogSoftmax (6, 1)
mono-BiGRU	GRU	torch.nn.GRU (7, 280)
	FC	torch.nn.Linear (280, 6)
	SM	torch.nn.LogSoftmax (6, 1)

1

2

Network type	Layer name	Type (Dimension)
dual-FRNN	FRNN1	torch.nn.RNN (4, 140)
	FRNN2	torch.nn.RNN (3, 140)
	FC	torch.nn.Linear (280, 6)
	SM	torch.nn.LogSoftmax (6, 1)
dual-BiFRNN	FRNN1	torch.nn.RNN (4, 280)
	FRNN2	torch.nn.RNN (3, 280)
	FC	torch.nn.Linear (560, 6)
	SM	torch.nn.LogSoftmax (6, 1)
dual-LSTM	LSTM1	torch.nn.LSTM (4, 140)
	LSTM2	torch.nn.LSTM (3, 140)
	FC	torch.nn.Linear (280, 6)
	SM	torch.nn.LogSoftmax (6, 1)
dual-BiLSTM	LSTM1	torch.nn.LSTM (4, 280)
	LSTM2	torch.nn.LSTM (3, 280)
	FC	torch.nn.Linear (560, 6)
	SM	torch.nn.LogSoftmax (6, 1)
dual-GRU	GRU1	torch.nn.GRU (4, 140)
	GRU2	torch.nn.GRU (3, 140)
	FC	torch.nn.Linear (280, 6)
	SM	torch.nn.LogSoftmax (6, 1)
dual-BiGRU	GRU1	torch.nn.GRU (4, 280)
	GRU2	torch.nn.GRU (3, 280)
	FC	torch.nn.Linear (560, 6)
	SM	torch.nn.LogSoftmax (6, 1)

1

2

1 **Table S4 Parameters used in MC simulations.**

Parameter type	Parameter name	Value/Dimension
Voxel geometry	Box size	120
	Tissue size	100
	Offset	10
	Voxel space	(120, 120, 120)
	LP radius*	15
Simulation configurations	# photon	10^7
	# materials	5
	Time step	10-12
	Simulation interval	2.5×10^{-10}
Light source parameters	Source type	zgaussian**
	Source parameter 1 (zenith angle)	20
	Source position	(60, 30, 9)
	Source direction	(0, 0, 1)
Optical parameters [μ_s , μ_a , g, n]	Background	[0, 0, 1, 1]
	Epidermis	[33.6, 0.80, 0.89, 1.31]
	Dermis	[20.1, 0.83, 0.89, 1.31]
	Subcutaneous fat	[18.5, 0.95, 0.89, 1.44]
	Muscle	[6.21, 0.32, 0.89, 1.37]

2 *Only used in MC simulations involving LP positioning.

3 **ZGaussian distribution is used to simulate the actualy Lambertian distribution, see Note S2 and
4 Figure S43.

5

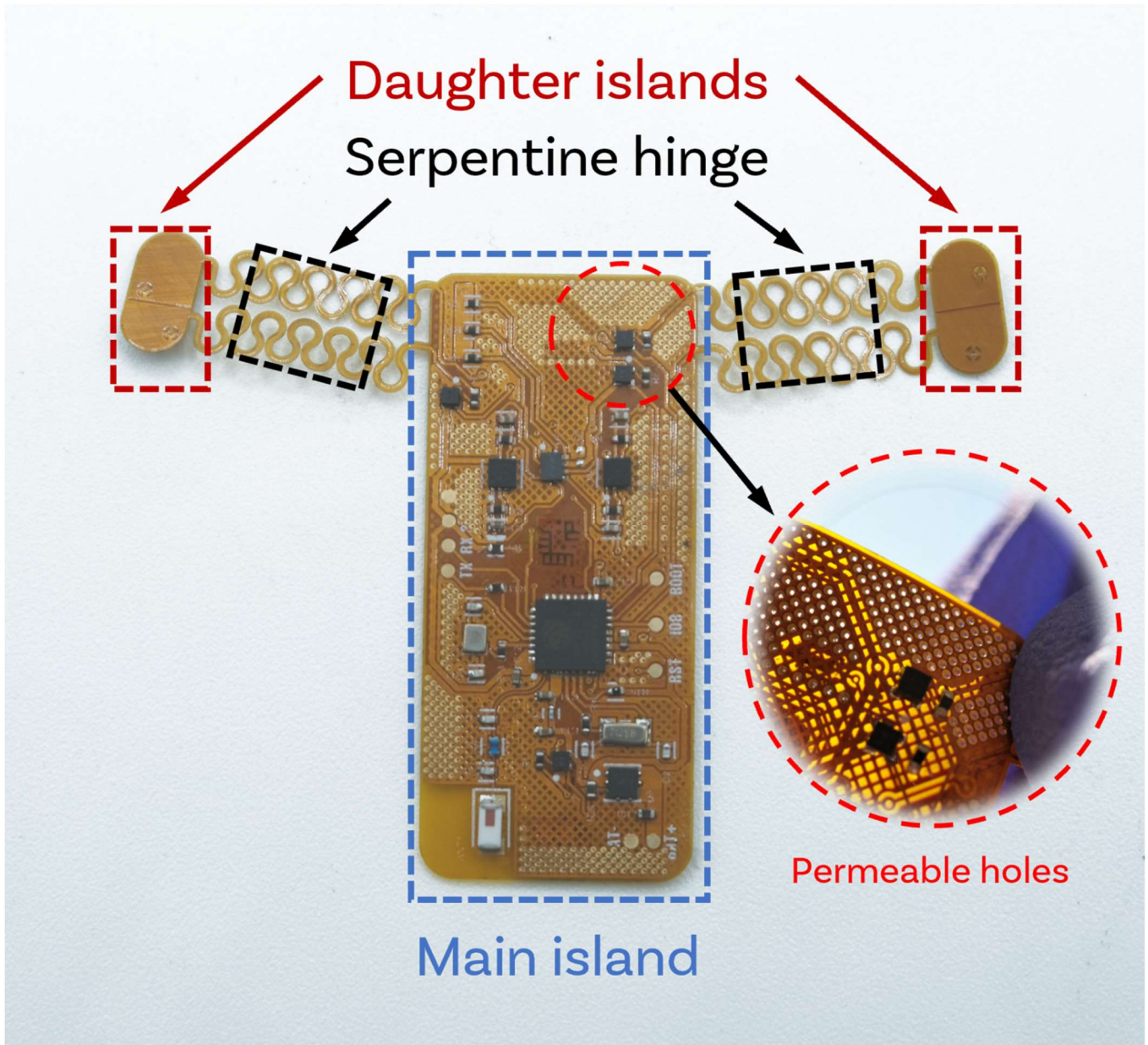
1 **Table S5 Parameters used in the training of dual-GRU and adap-GRU.**

Network	Parameter name	Value
dual-GRU	Epoch number	400
	Early stop	200
	Hidden layer depth	140
	Learning rate	0.0001
	Regularization	weight decay (0.01) dropout (0.1)
adap-GRU	Epoch number	50
	Early stop	25
	Hidden layer depth	140
	Learning rate	0.005
	Regularization	weight decay (0.01) dropout (0.1)

2

3

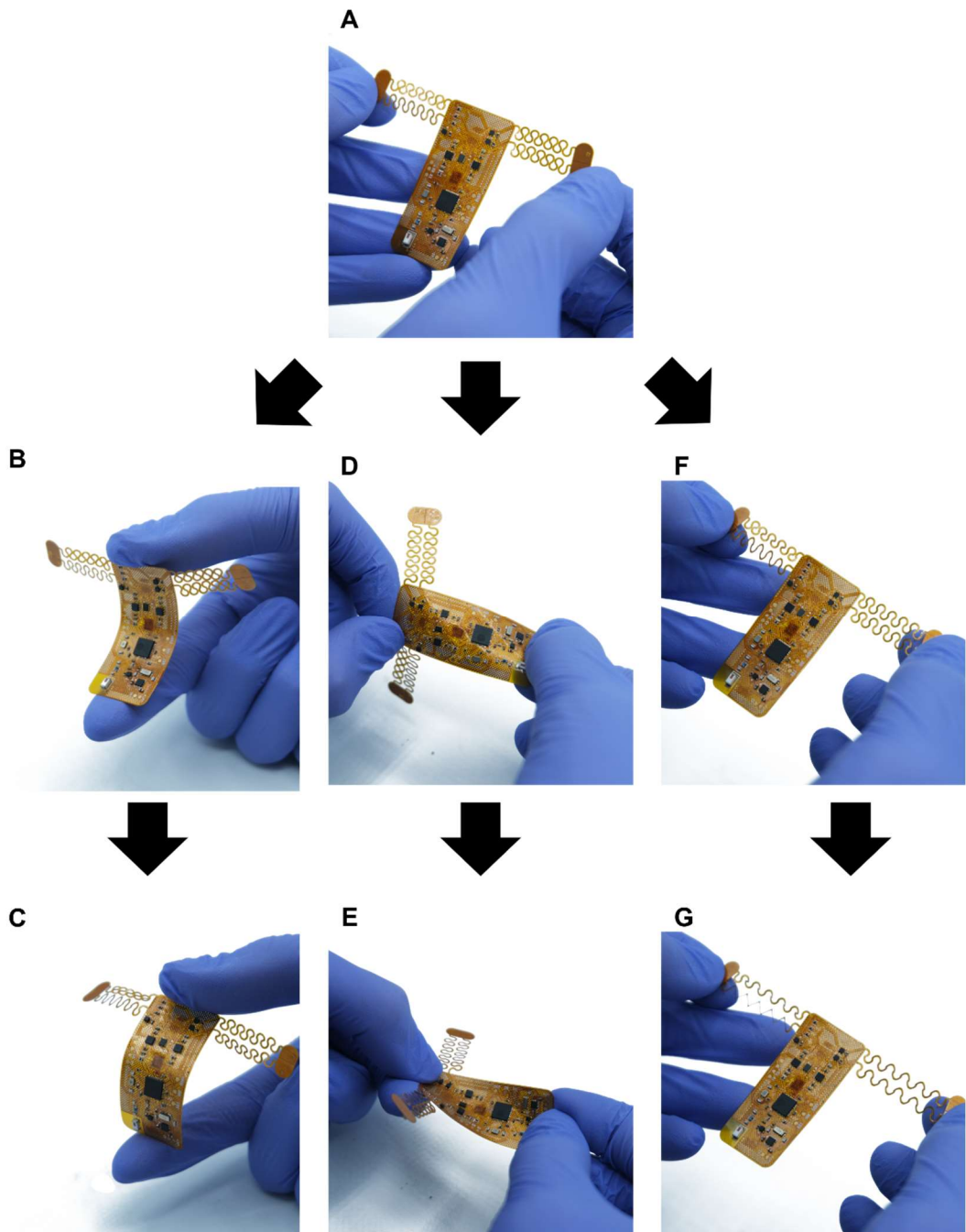
1 Supplementary Figures



2

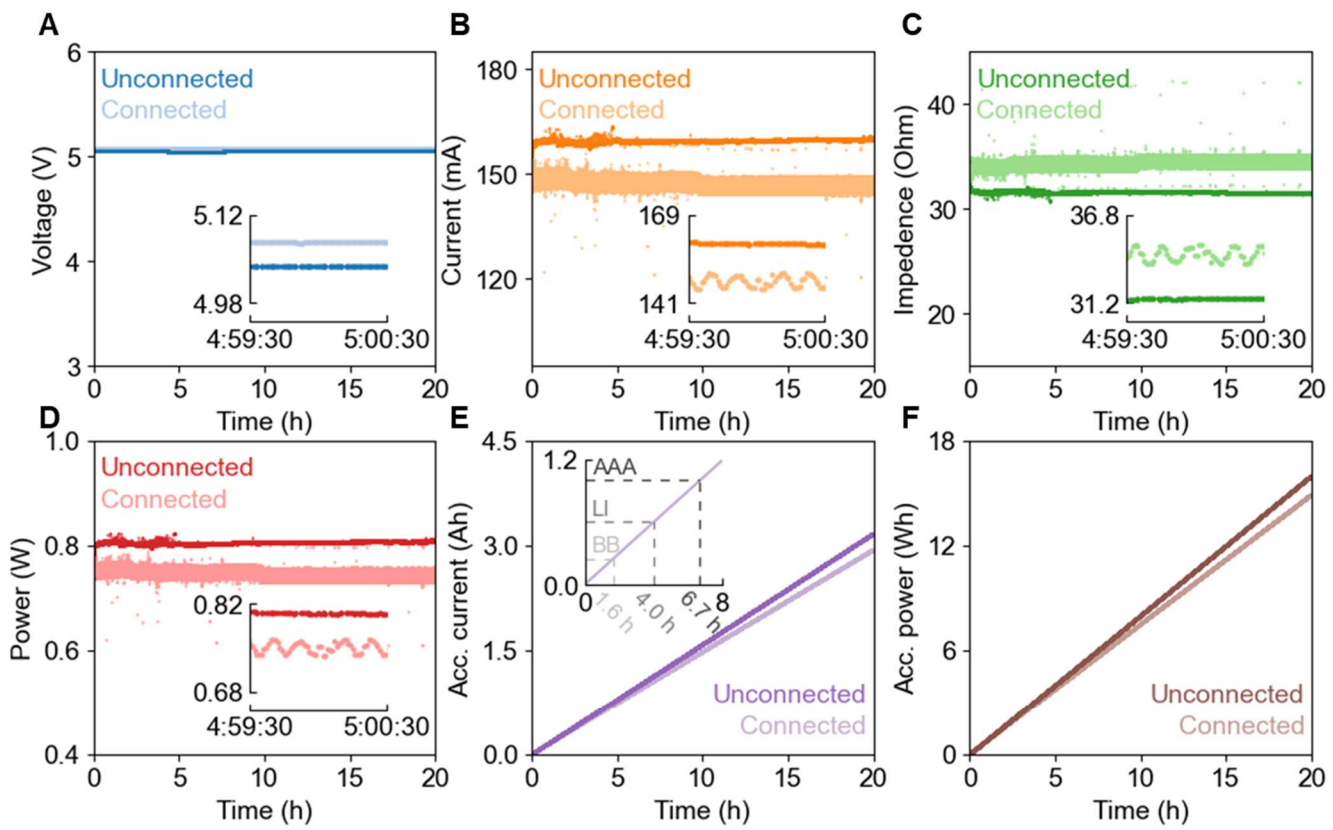
3 **Figure S1** Three regions of the design. A main PCB hinge, consisting of 10 serpentine traces, connects
4 the control island to the sensing island. Two more hinges connect the sub-islands to the main sensing
5 island. Inset highlights the permeable holes on the PCB.

6



1

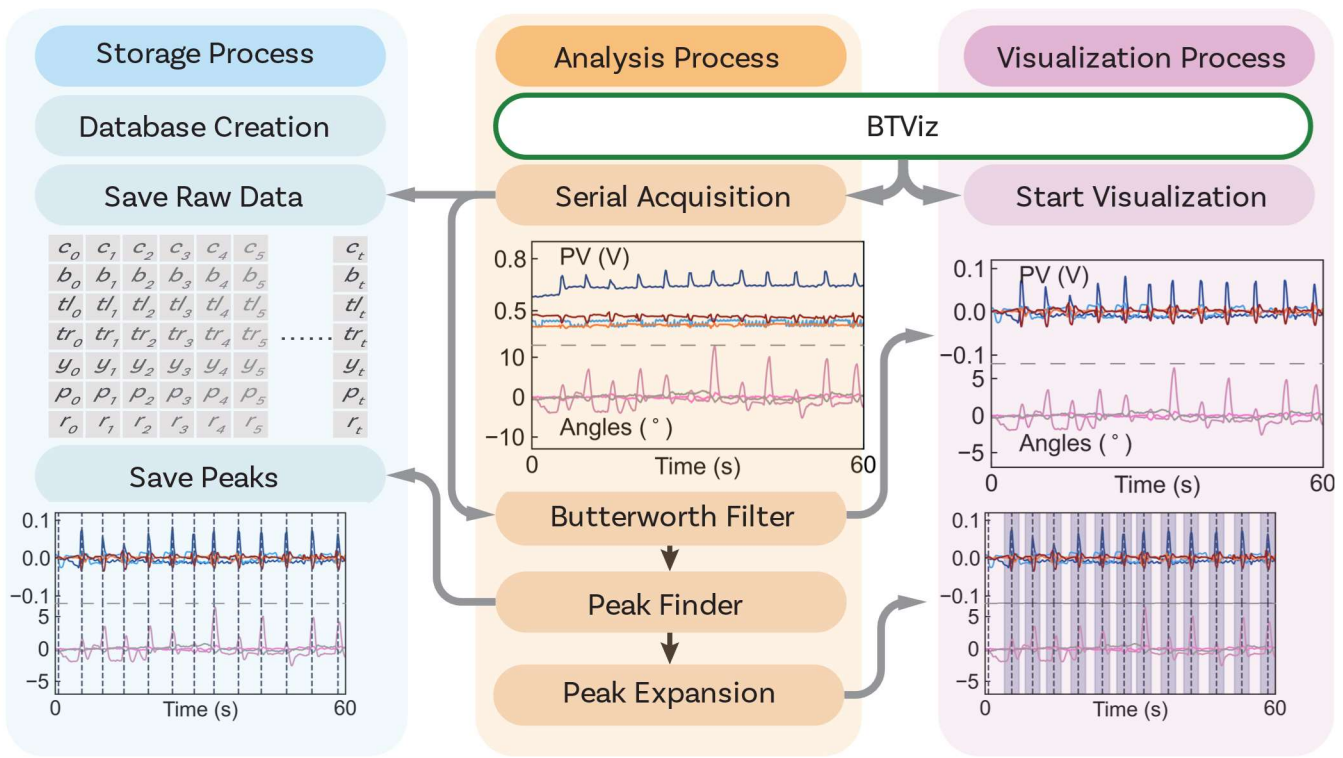
2 **Figure S2** Demonstration of the durability of the PCB against different deformations. (A) The original
3 shape. (B) A 45-degree twisting around the long axis of the patch. (C) A 90-degree twisting around the
4 short axis of the patch. (D) A 90-degree buckling around the hinge structure. (E) A 180-degree buckling
5 around the hinge structure. (F) Same as (E), shown in a different view. (G) A further incurve around the
6 long axis after the 180-buckling around the hinge structure.



1

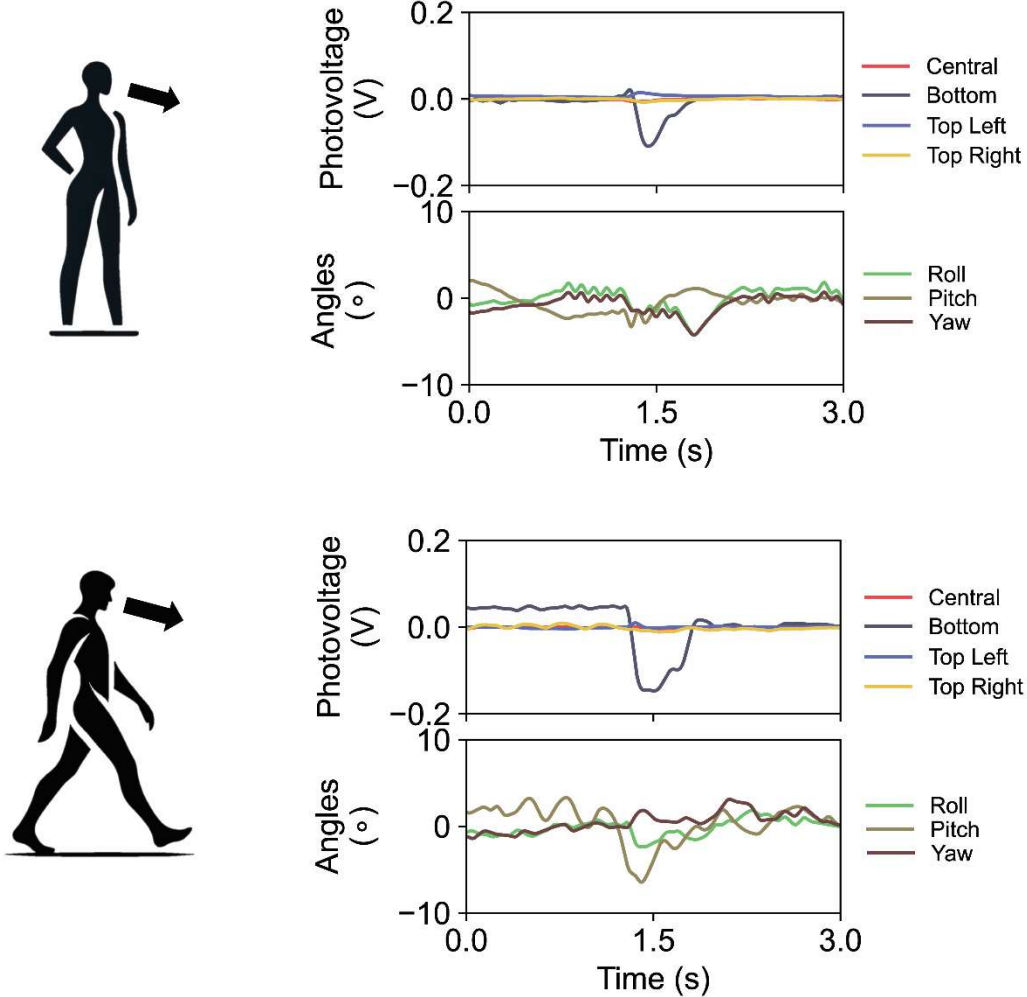
2 **Figure S3** Power consumption test. Each subplot shows both the power consumption at connected
 3 status (lighter color) and disconnected status (darker color). Insets in (A-D) highlight the measured
 4 values of a 1-minute slice at the 5-hour timepoint. (A) Voltage supply. (B) Current consumption. (C) Port
 5 impedance. (D) Power consumption. (E) Accumulated current. Inset shows the accumulated current
 6 change in the first 8 hours. The calculated last time of the commonly used power source button battery
 7 (BB), lithium-ion battery (Li) and AAA battery are labelled in the inset. (F) Accumulated power.

8



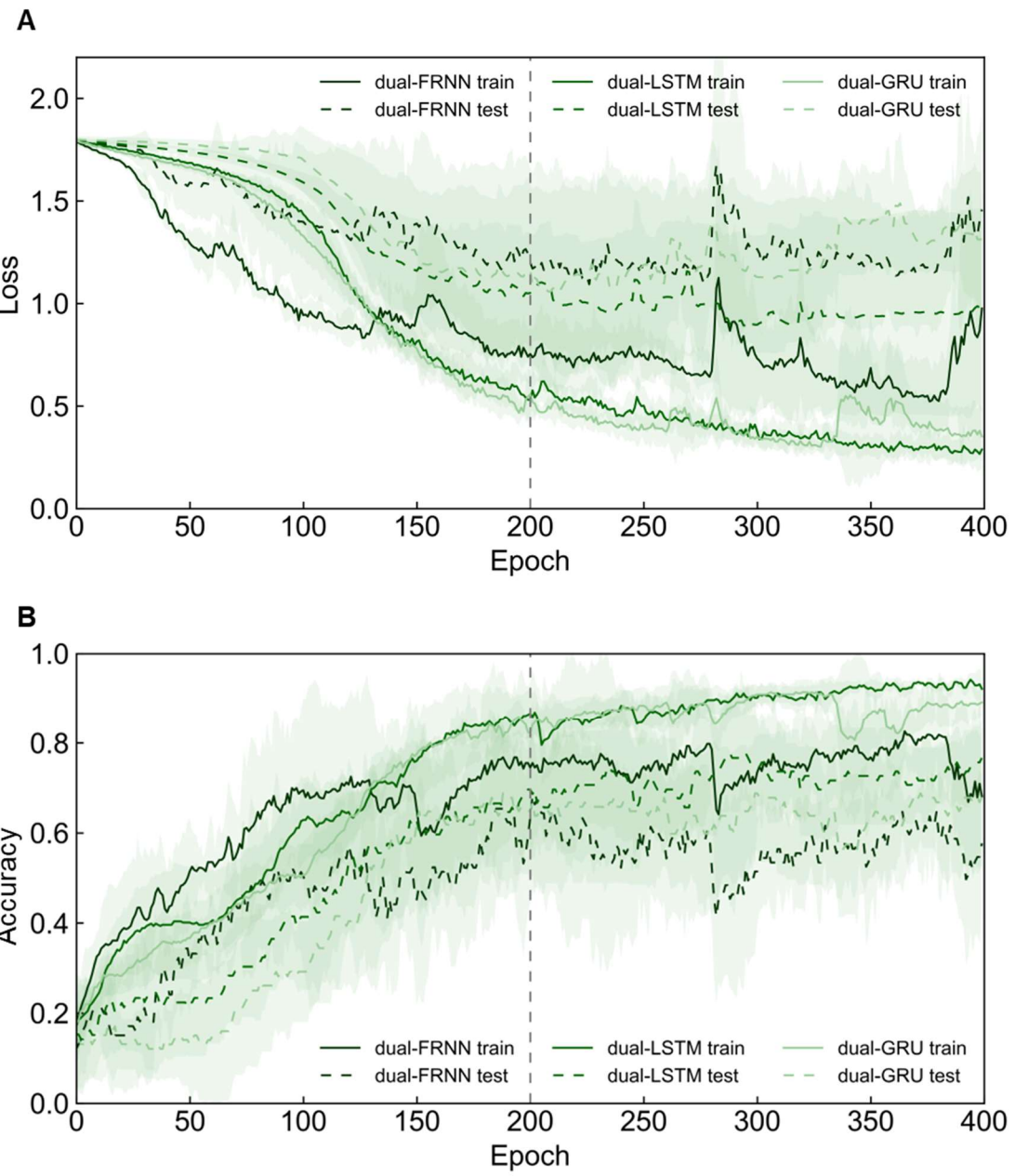
1

2 **Figure S4** Visual depiction of workflow in data preprocessing including data storage, analysis and
 3 visualization. The process starts with the storage of raw data and signal peaks, followed by continuous
 4 processing and peak analysis of acquired data, and then completes the real-time visualization of
 5 processed data.



1

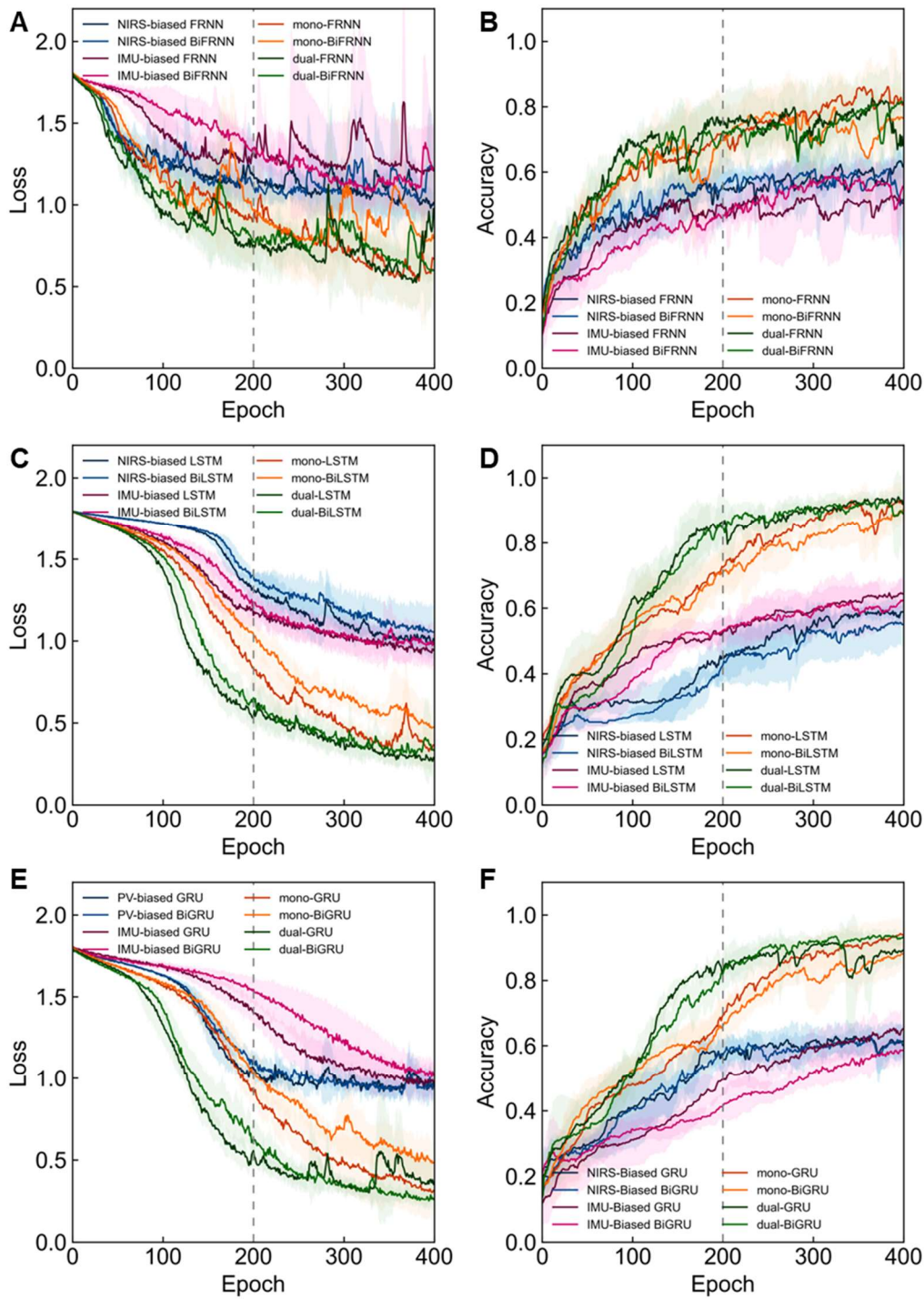
2 **Figure S5** Comparison of LaHMo data between one dry cough event while standing still (top)
 3 and while walking (bottom).



1

2 **Figure S6** Comparison between training and testing sets during the training of dual-FRNN, dual-LSTM,
3 and dual-GRU. (A) Loss curve. (B) Accuracy curve.

4

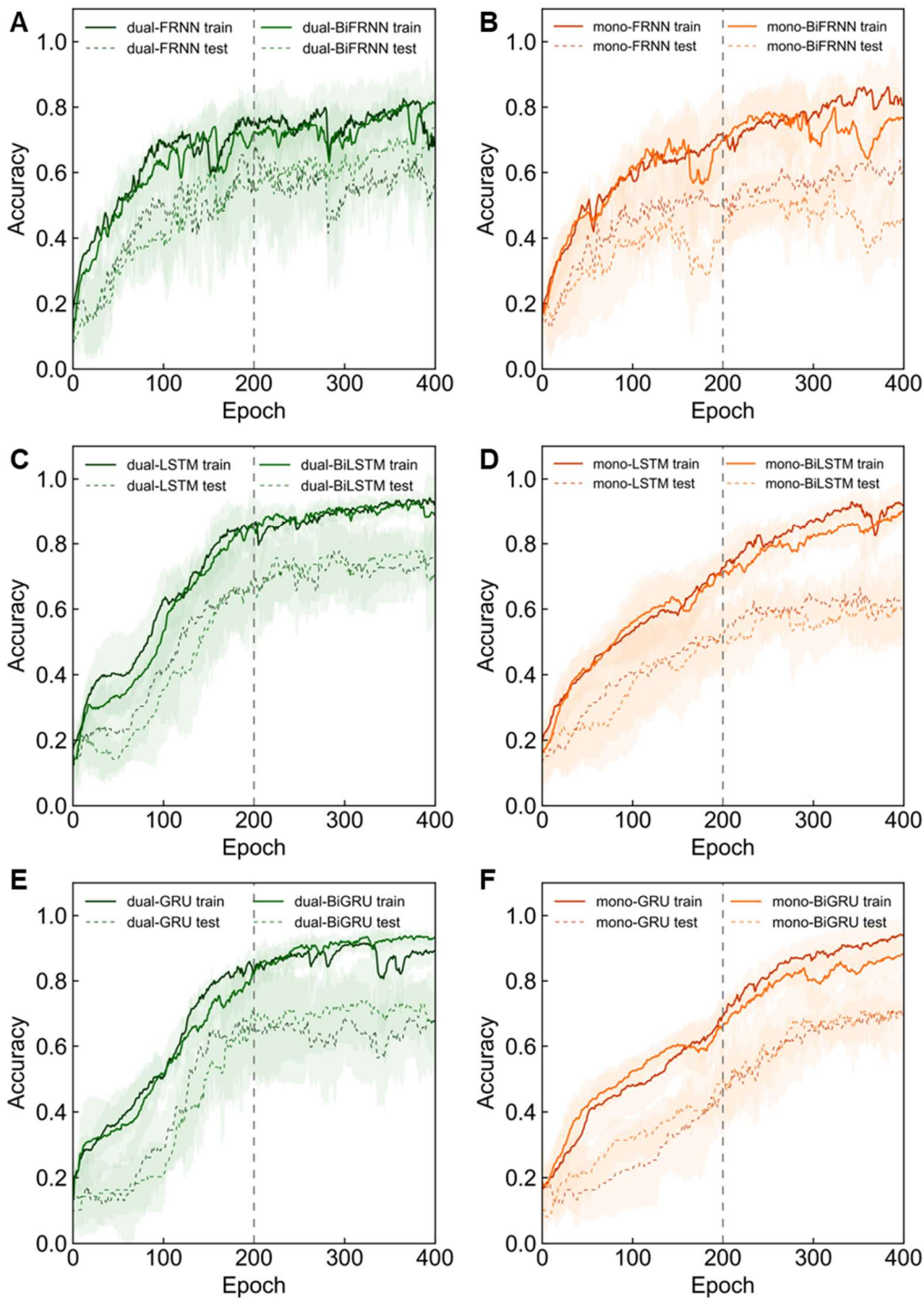


1

2 **Figure S7** Training curves for FRNN (A-B), LSTM (C-D), and GRU (E-F), respectively. Different colors
 3 show different architectures. The loss curves are shown on the left (A, C, E), and the accuracy curves
 4 are shown on the right (B, D, F)

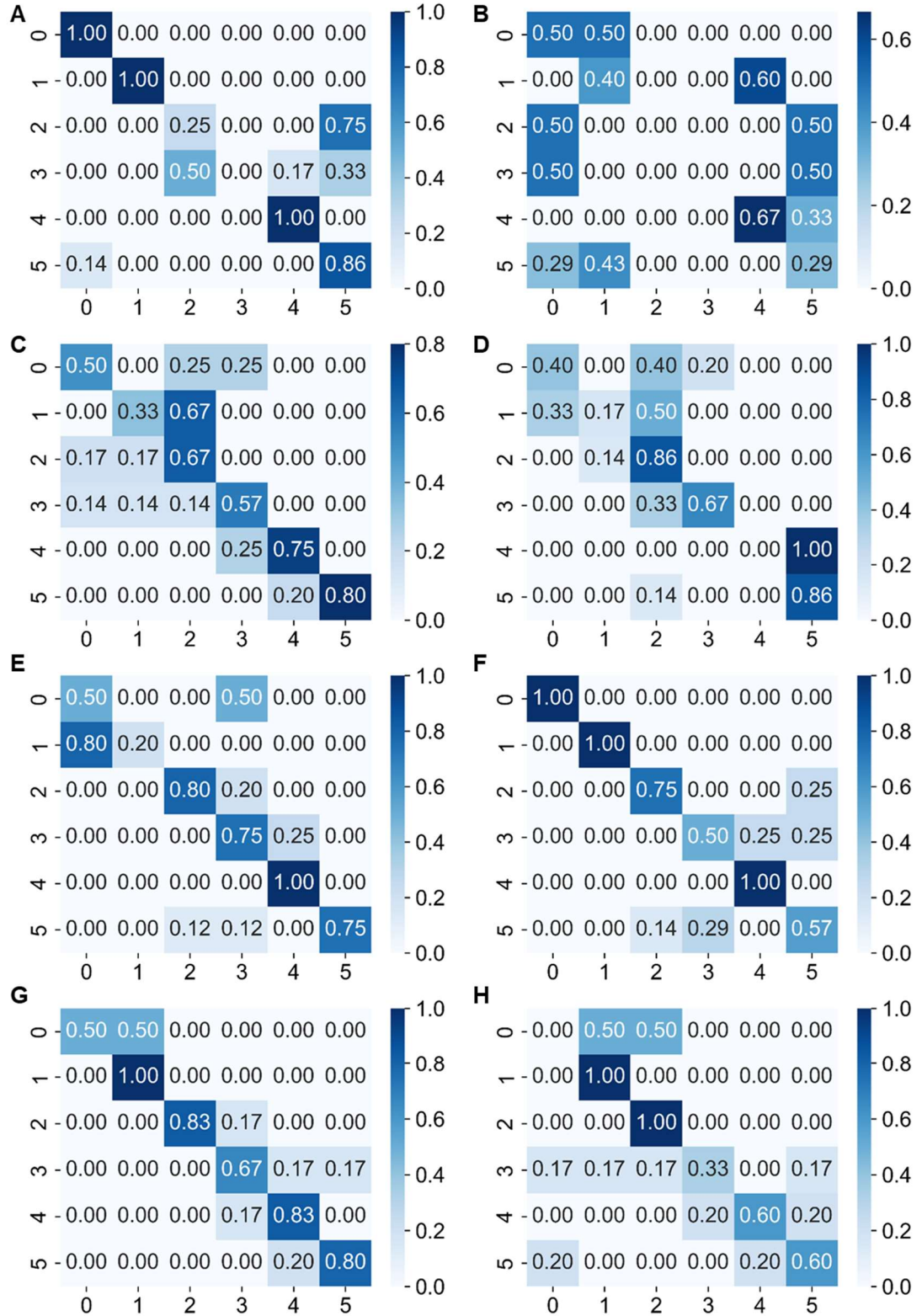
5

1



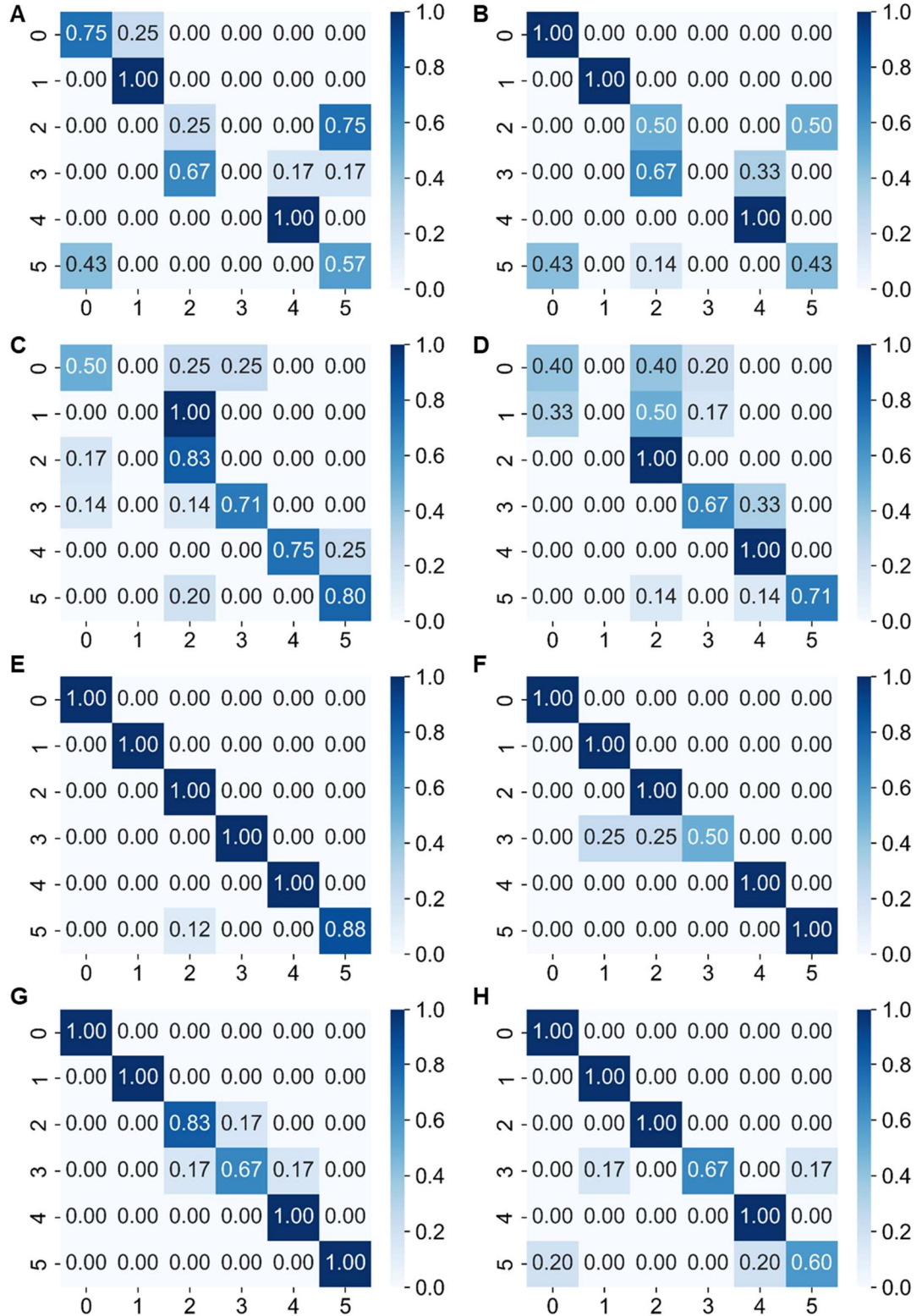
2

3 **Figure S8** Comparison between the training curves between RNN models and their bidirectional
 4 variants. (A, C, E) accuracy curves for three dual-RNNs and dual-BiRNNs. (B, D, F) accuracy curves
 5 for three mono-RNNs and mono-BiRNNs.



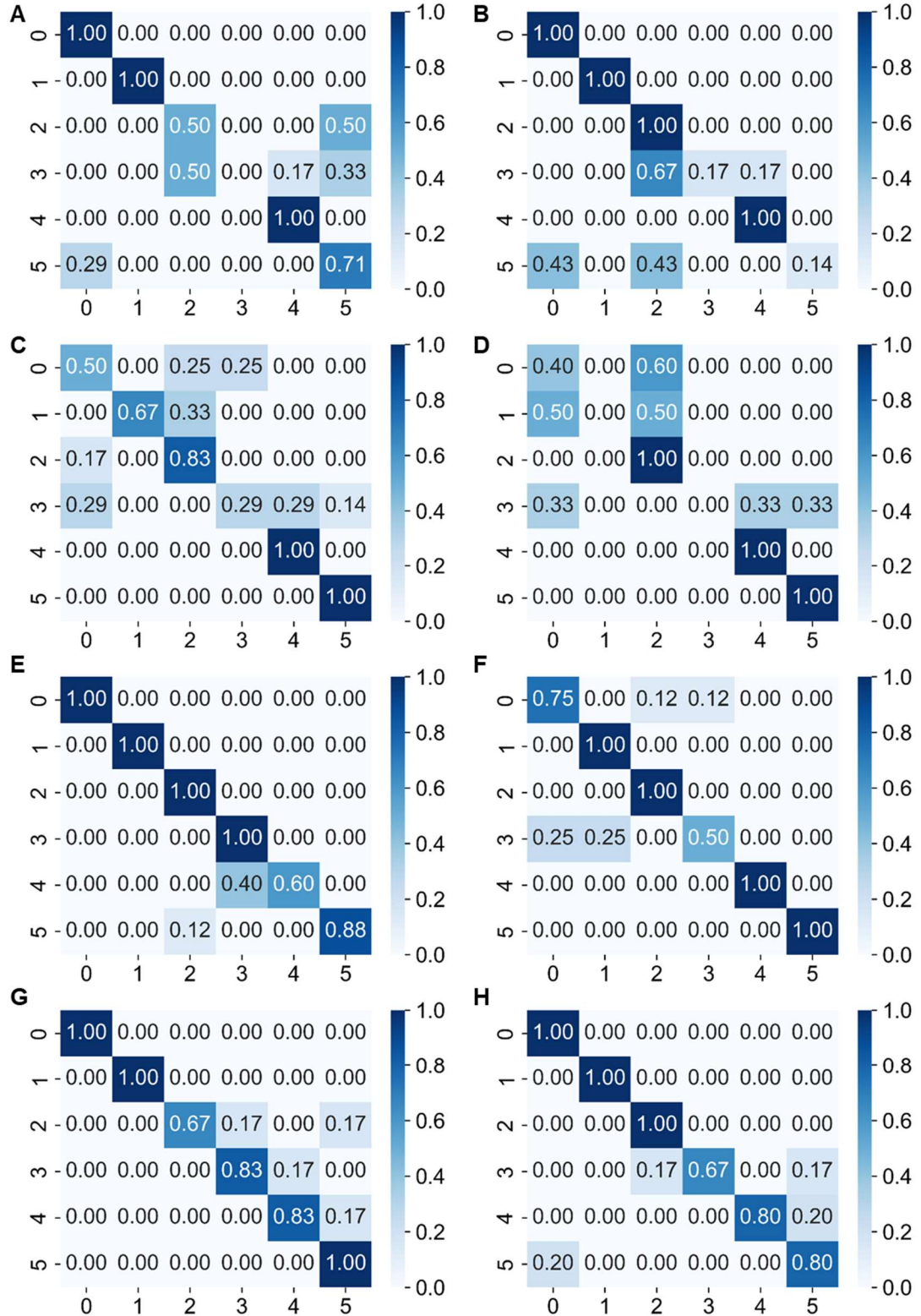
1

Figure S9 Confusion matrix for FRNN models on testing dataset. (A) PV-biased FRNN. (B) PV-biased BiFRNN. (C) IMU-biased FRNN. (D) IMU-biased BiFRNN. (E) mono-FRNN. (F) mono-BiFRNN. (G) dual-FRNN. (H) dual-BiFRNN.



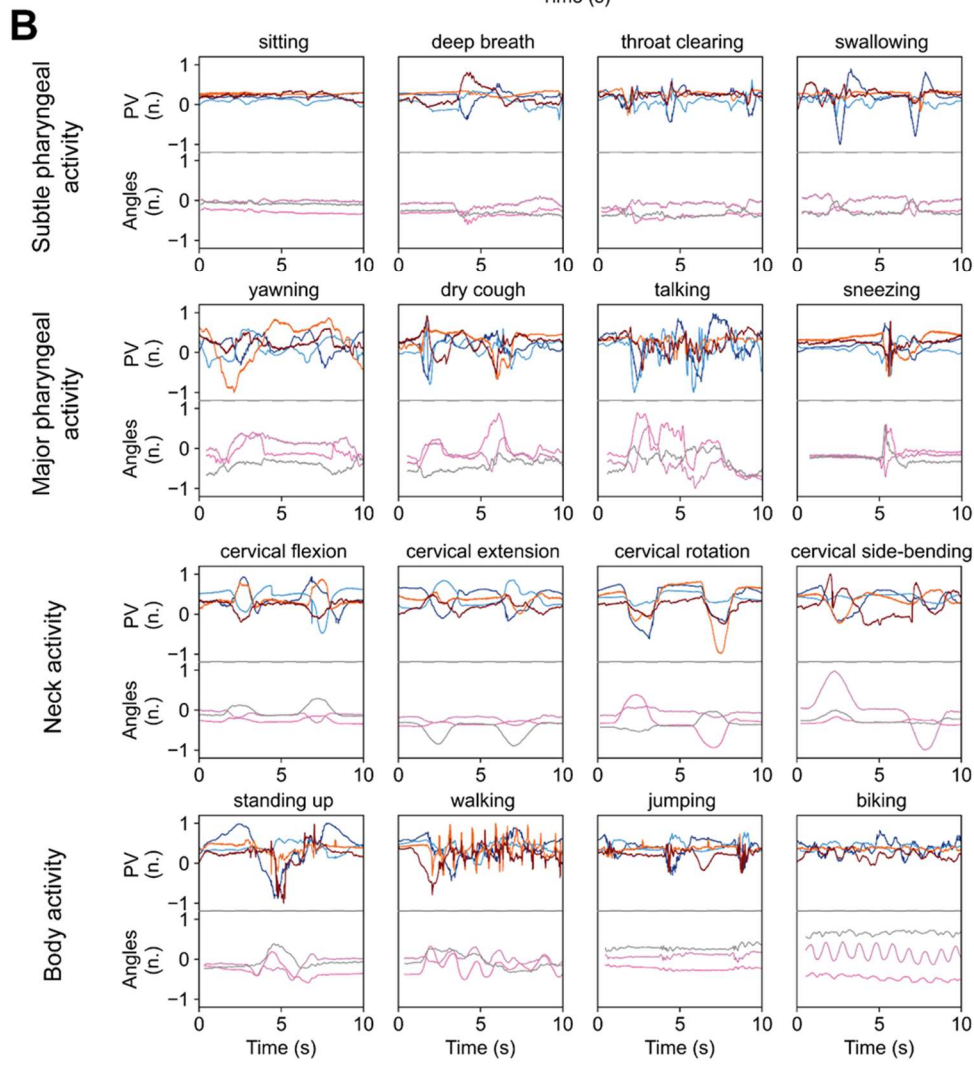
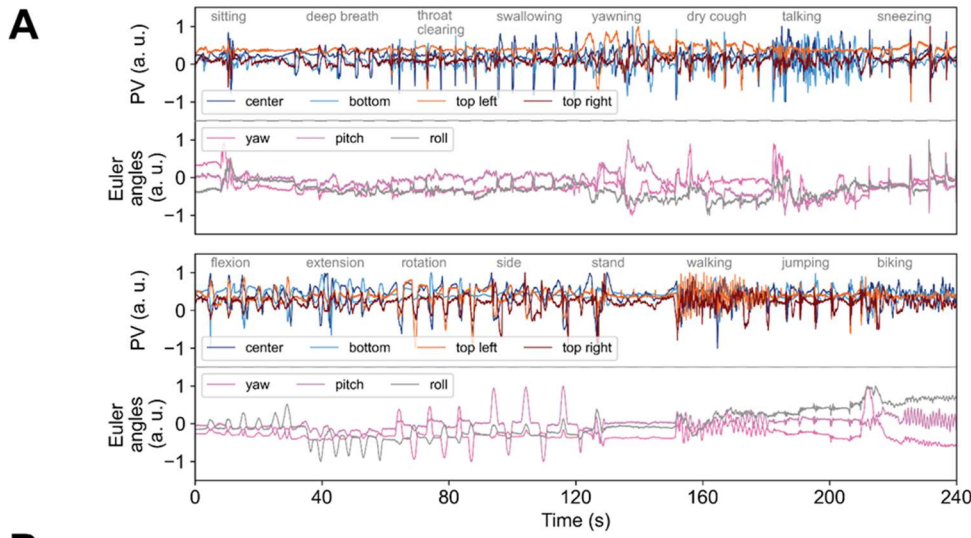
1

Figure S10 Confusion matrix for LSTM models on testing dataset. (A) PV-biased LSTM. (B) PV-biased BiLSTM. (C) IMU-biased LSTM. (D) IMU-biased BiLSTM. (E) mono-FRNN. (F) mono-BiLSTM. (G) dual-LSTM. (H) dual-BiLSTM.



1

Figure S11 Confusion matrix for GRU models on testing dataset. (A) PV-biased GRU. (B) PV-biased BiGRU. (C) IMU-biased GRU. (D) IMU-biased BiGRU. (E) mono-GRU. (F) mono-BiGRU. (G) dual-GRU. (H) dual-BiGRU.



1

2 **Figure S12** Extended tests with a LaHMo on various activities. 16 types of physiological activities are
3 classified into four groups to show their distinct pattern signatures in the data collected from the
4 wearable patch.

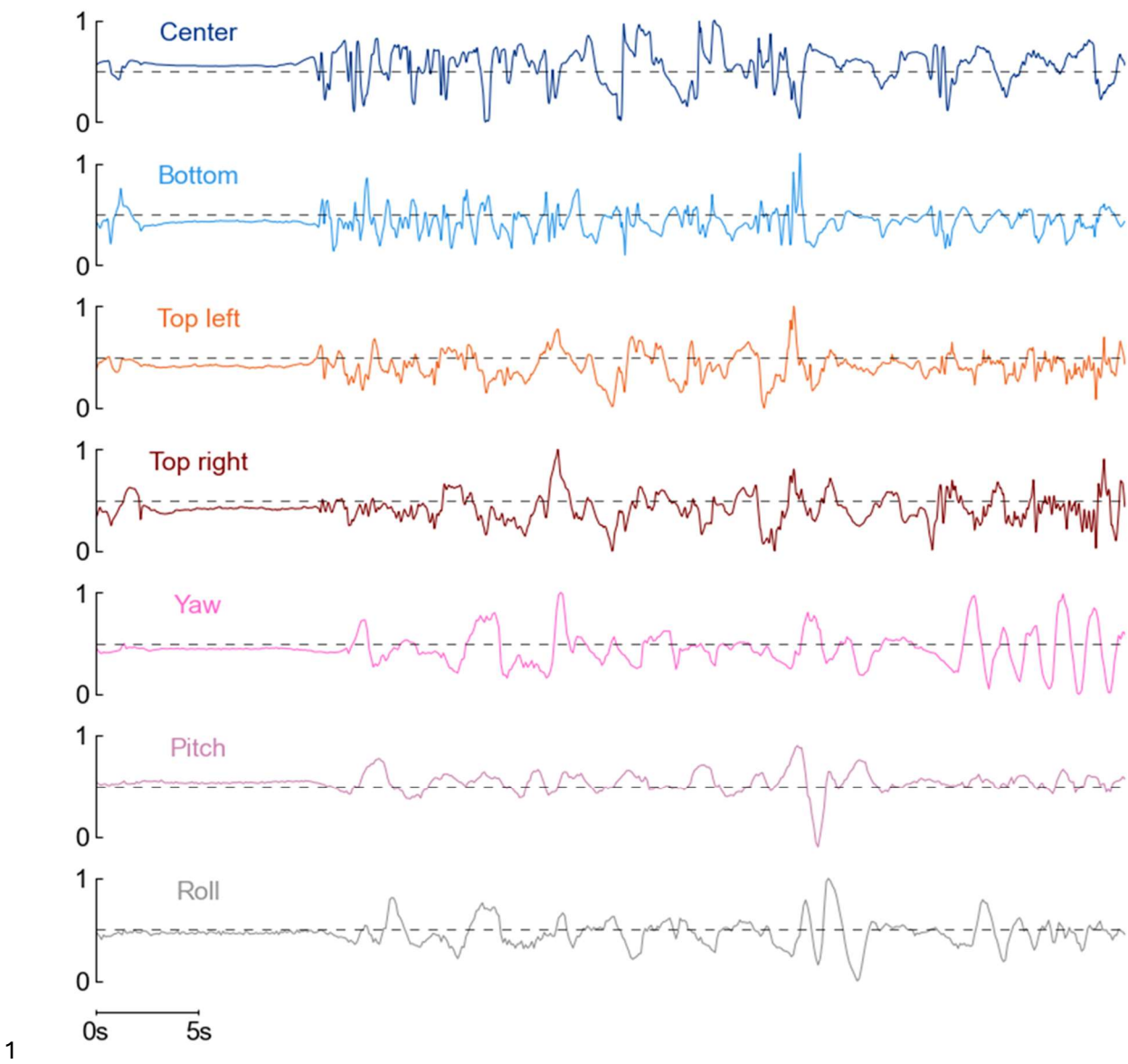
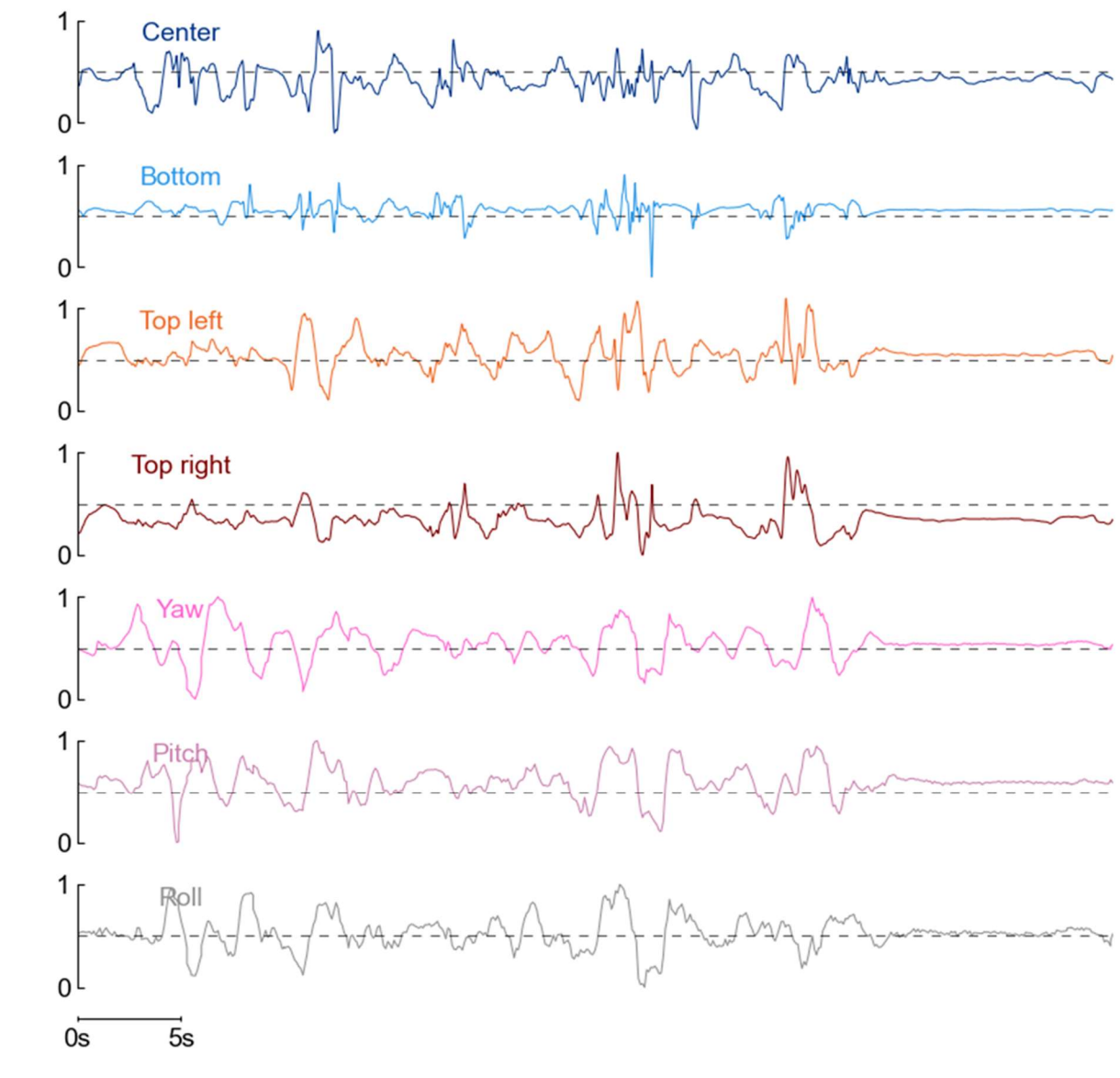


Figure S13 Continuous dry cough test. Photodiode response of LaHMo to continuous dry coughs, with minimal time and no recovery between coughs.



1
2 **Figure S14** Random dry cough test. Photodiode response of LaHMo to random dry coughs, with
3 varying amounts of time and recovery between coughs.
4

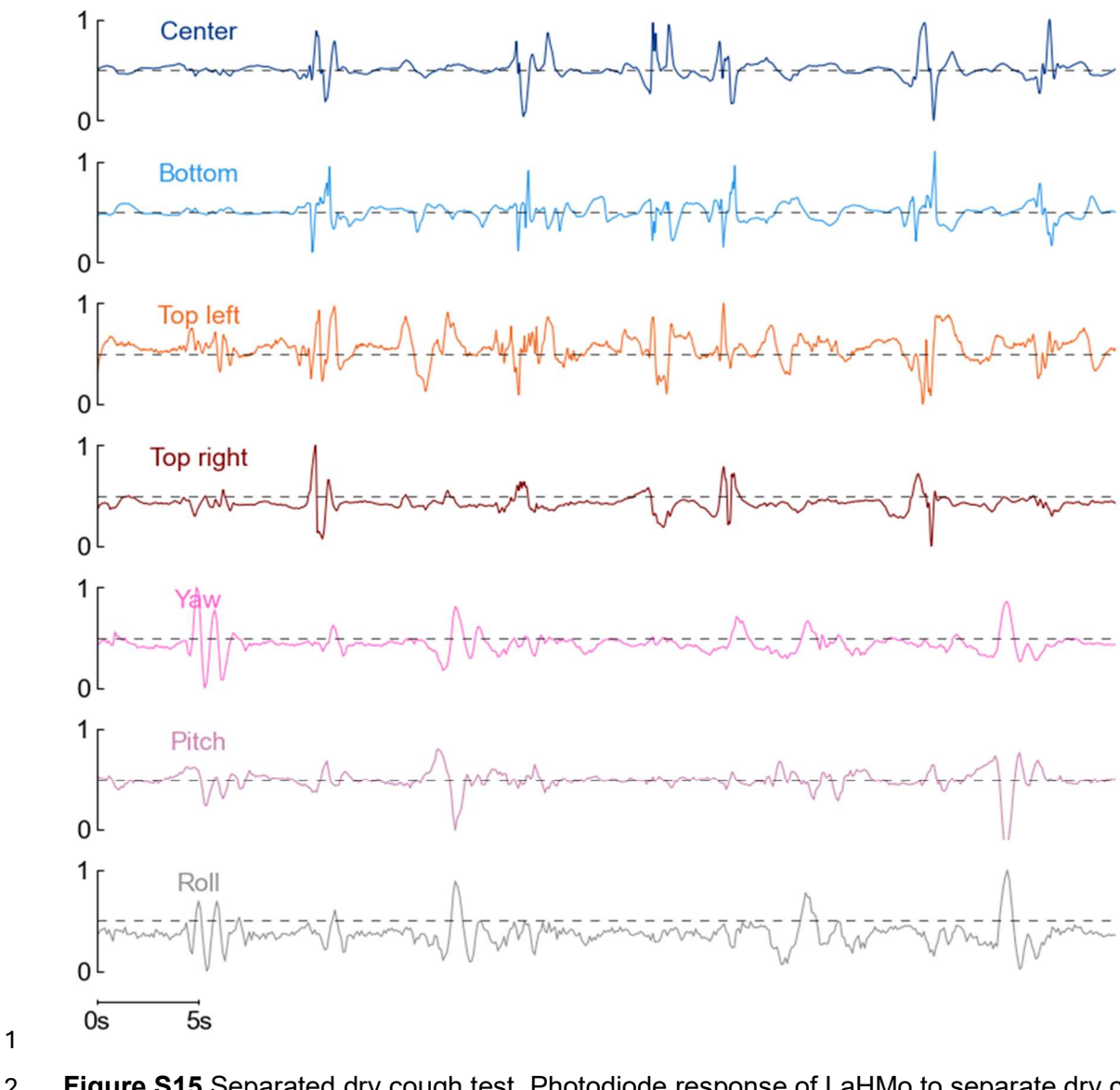
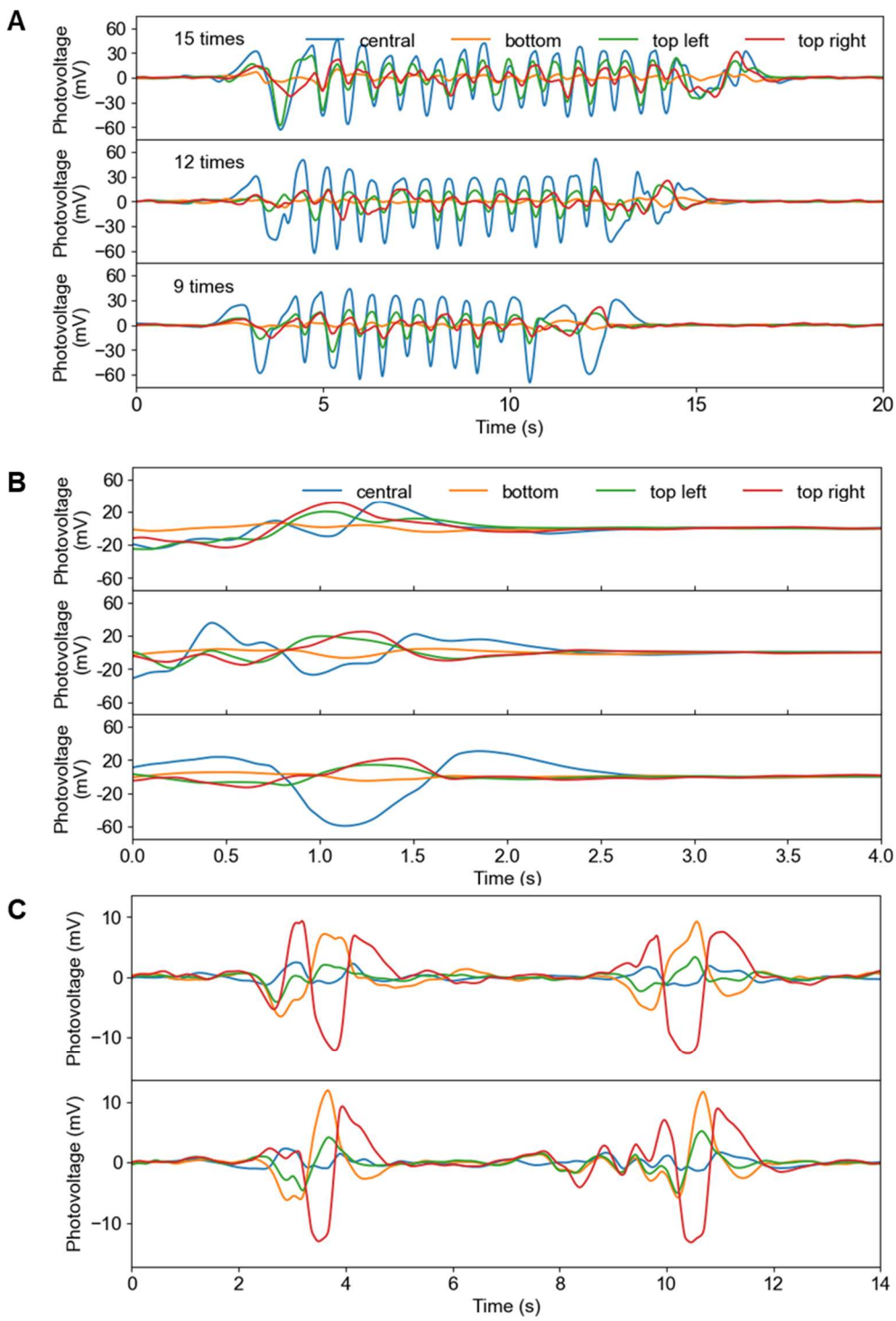
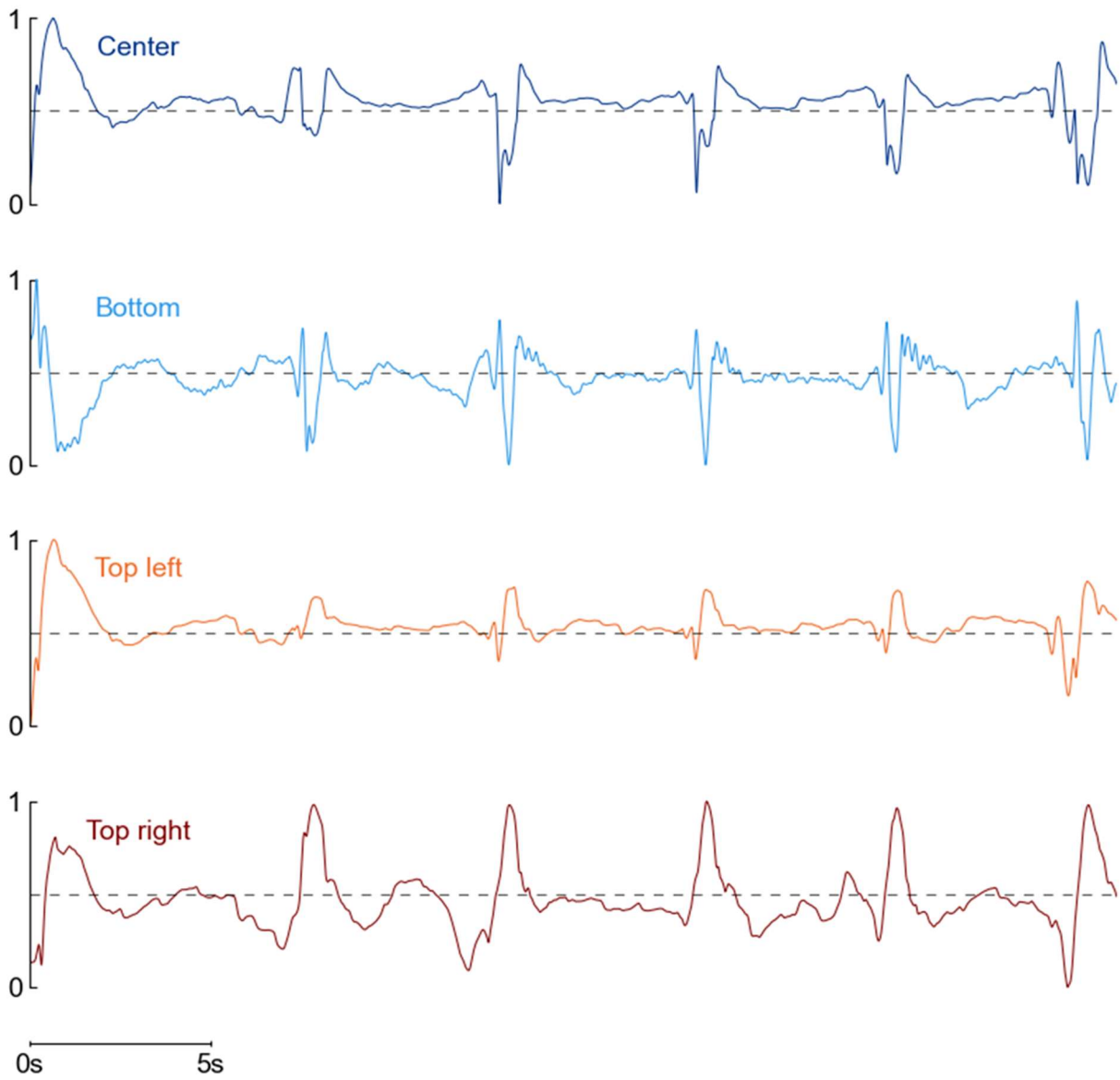


Figure S15 Separated dry cough test. Photodiode response of LaHMo to separate dry coughs, with enough time to allow for complete recovery between coughs.

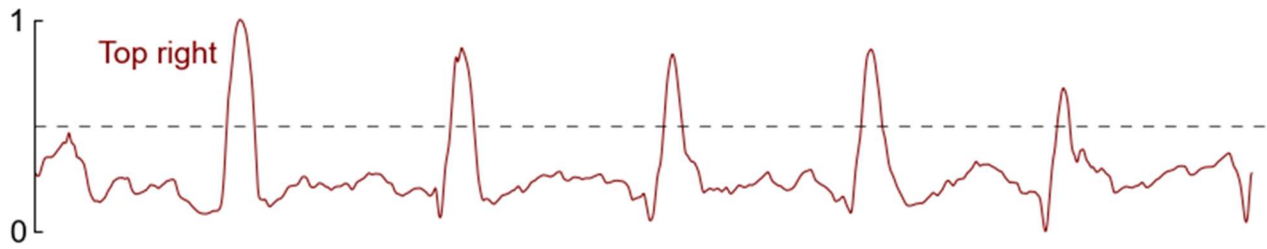
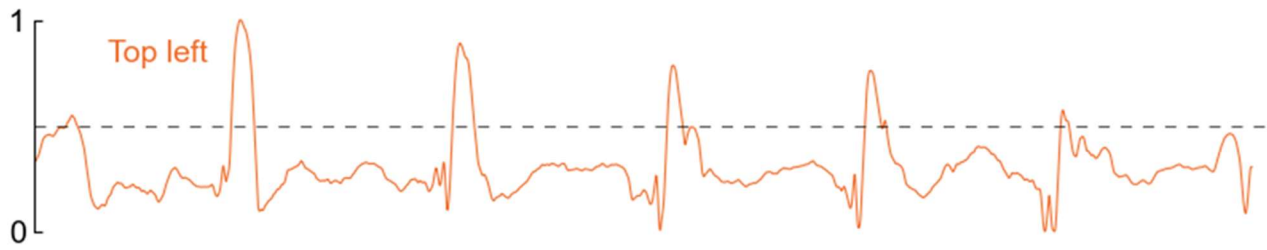
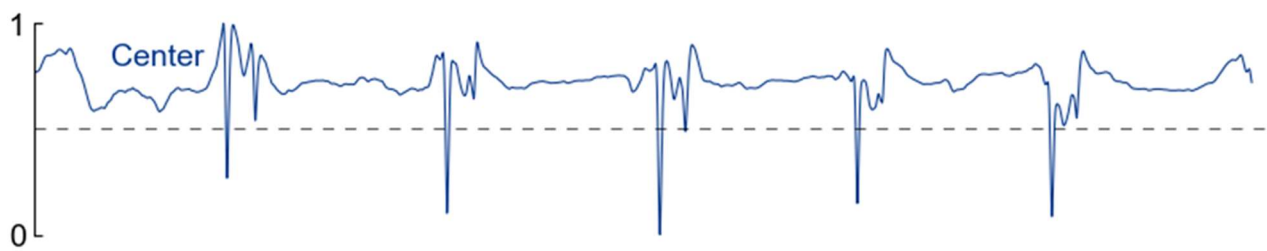


1

2 **Figure S16** Comparison of the photodiode response of LaHMo to various swallow qualities. (A)
3 Response to different chewing times (same food sample). From top to bottom: 15 chews, 12 chews, 9
4 chews. (B) Enlarged view of (A) at the swallowing. (C) Continuous swallowing, top: sufficient swallow,
5 bottom: insufficient swallow (more muscle activities)

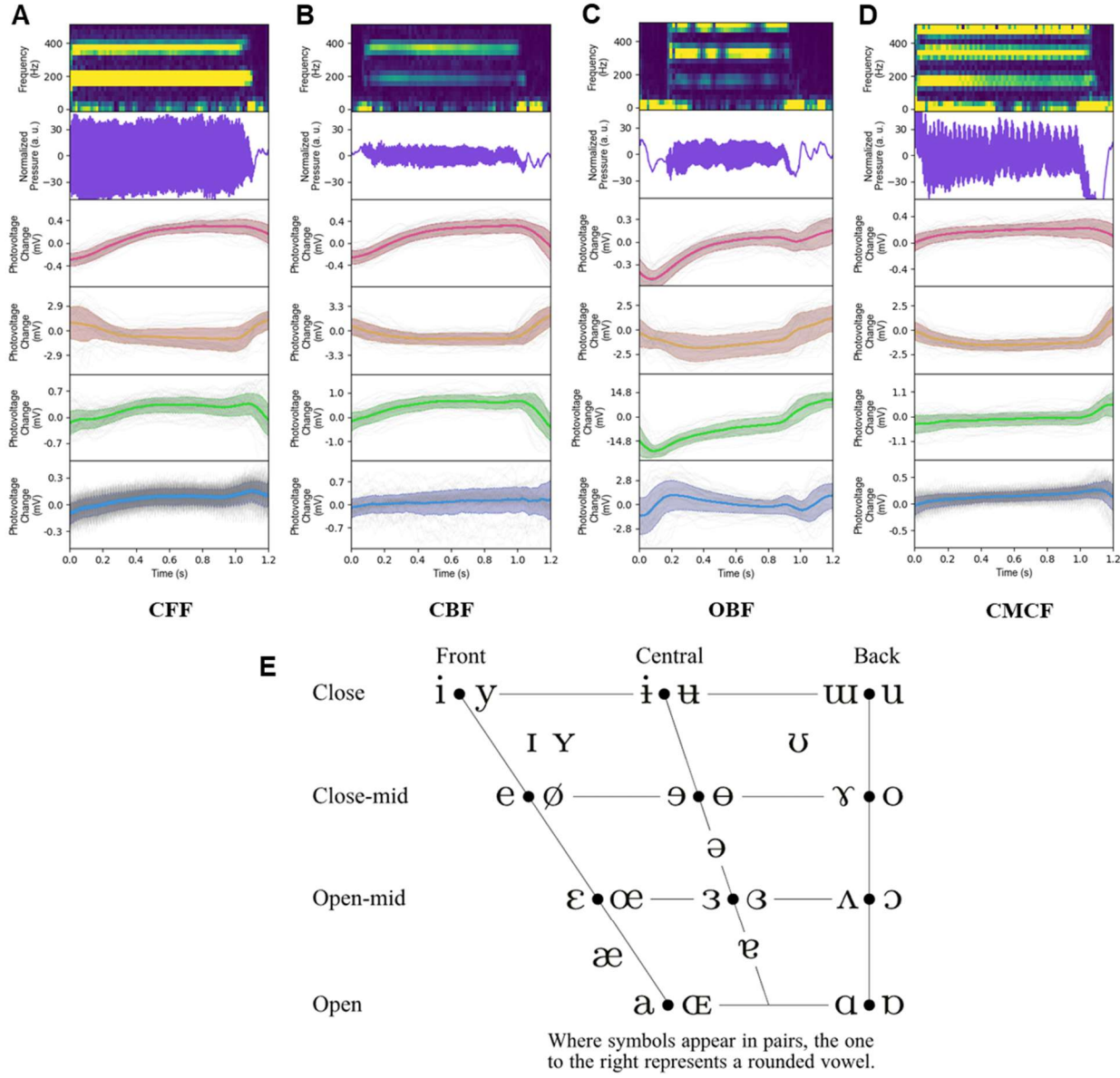


1
2 **Figure S17** Photodiode response of LaHMO to swallowing vegetable juice.
3



0s 5s

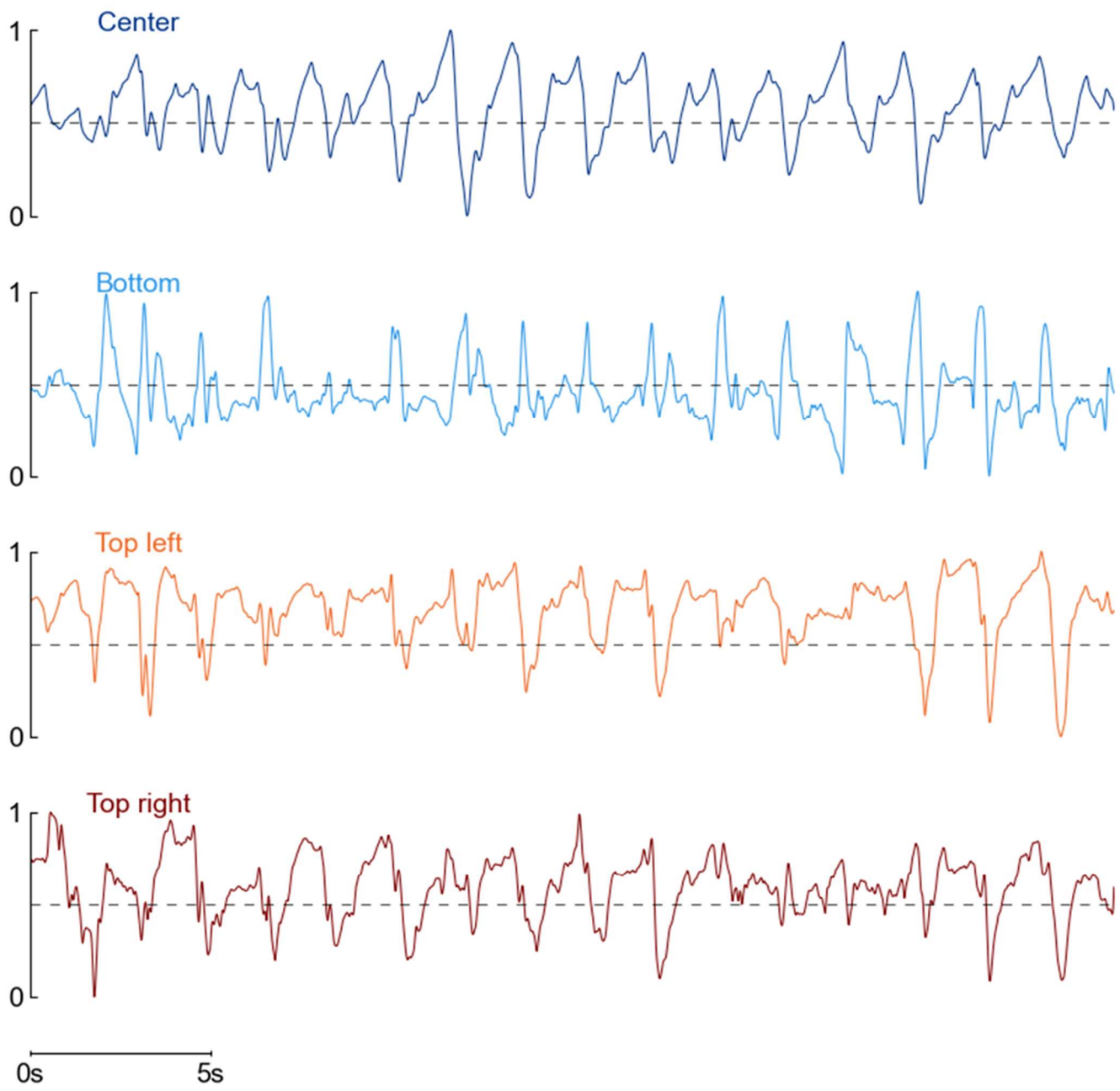
2 **Figure S18** Photodiode response of LaHMO to swallowing water.



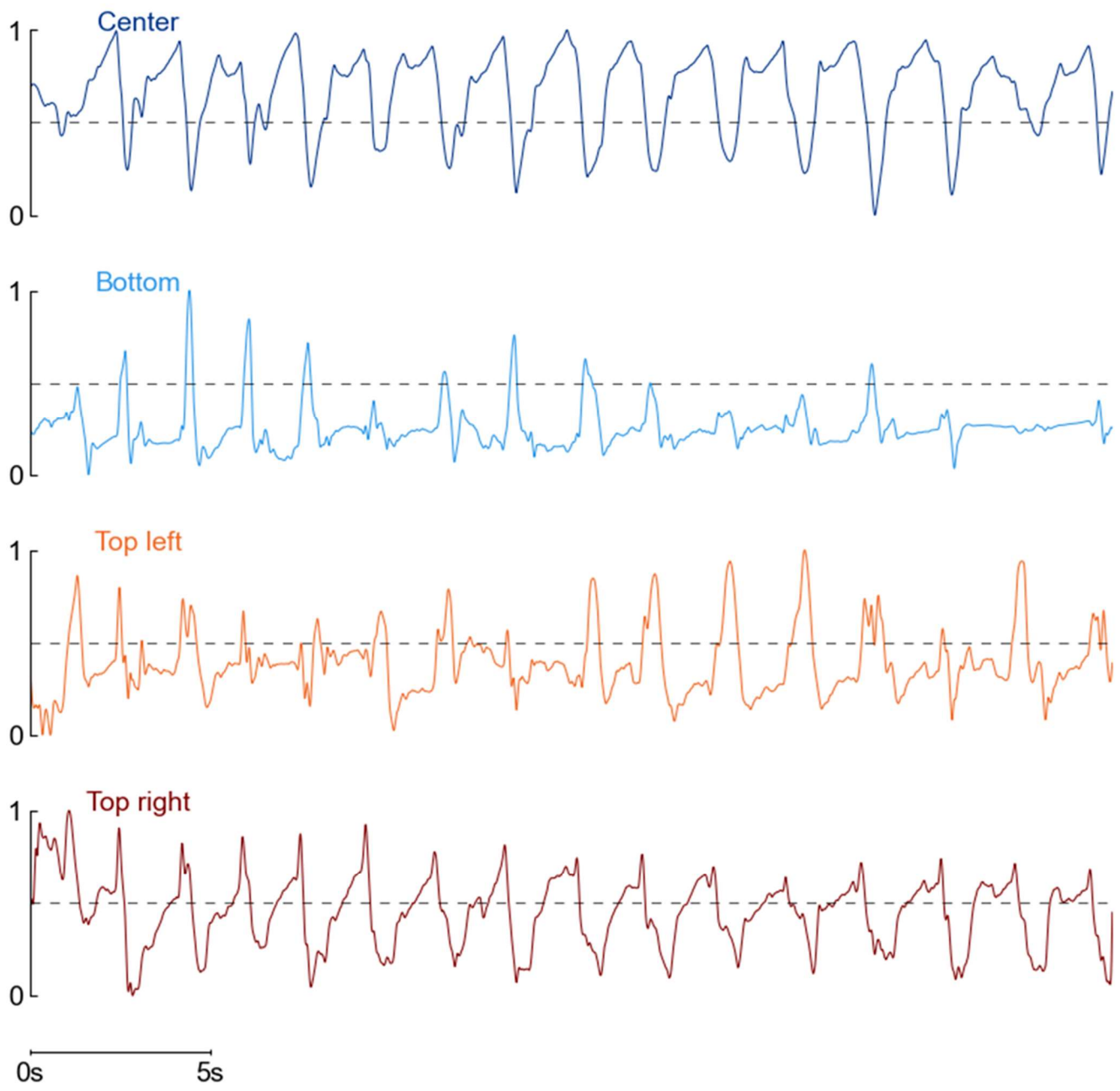
1

2 **Figure S19** Photovoltage response of LaHMo to various vowel phonemes. (A) Close front flat /i/. (B)
3 Close back flat /u/. (C) Open back flat /ɑ/. (D) Close-mid central flat /ə/. (E) Vowel location reference.
4 The horizontal axis shows the tongue peak anterior location, the vertical axis shows the mouth open
5 content.

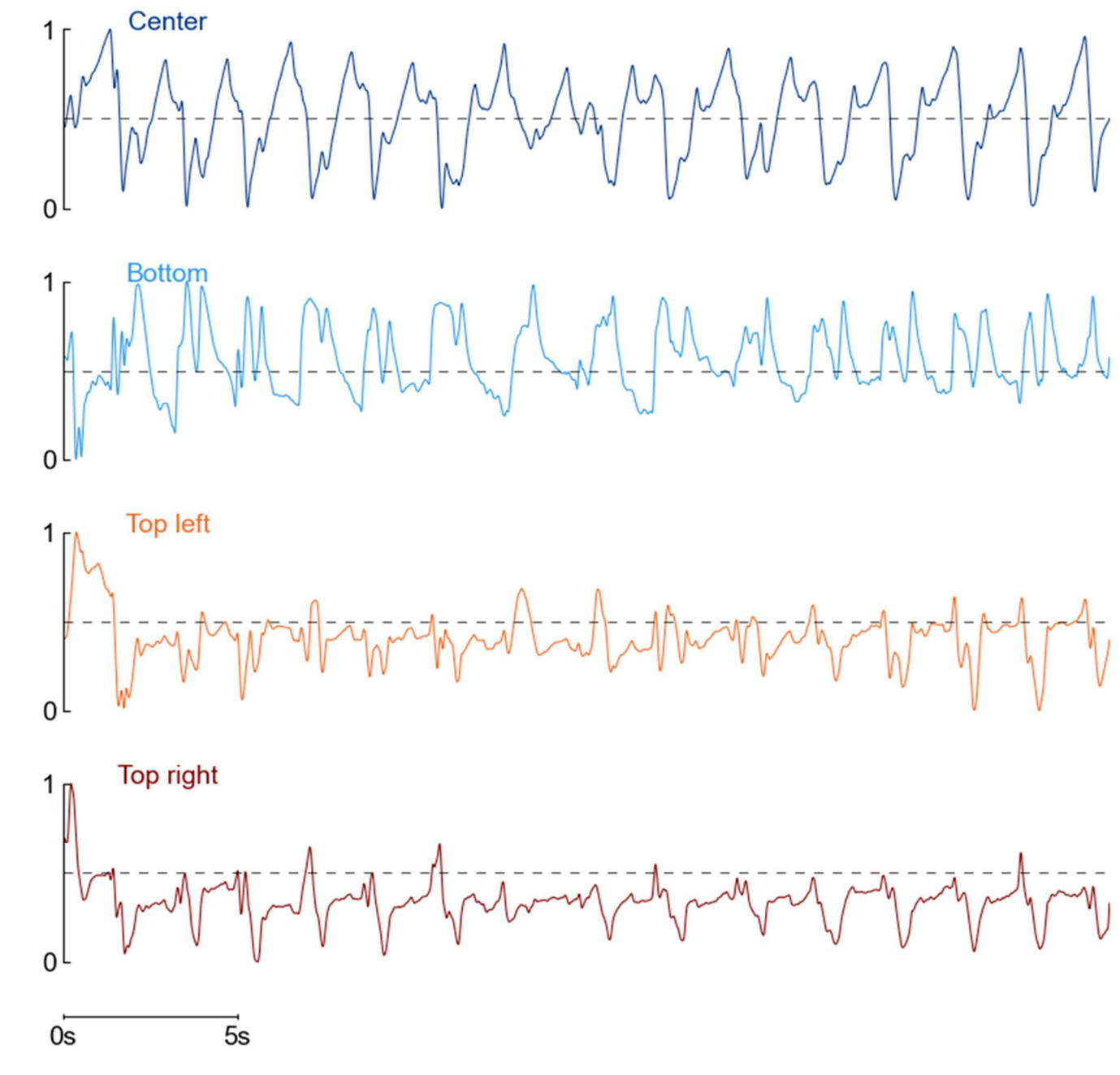
6



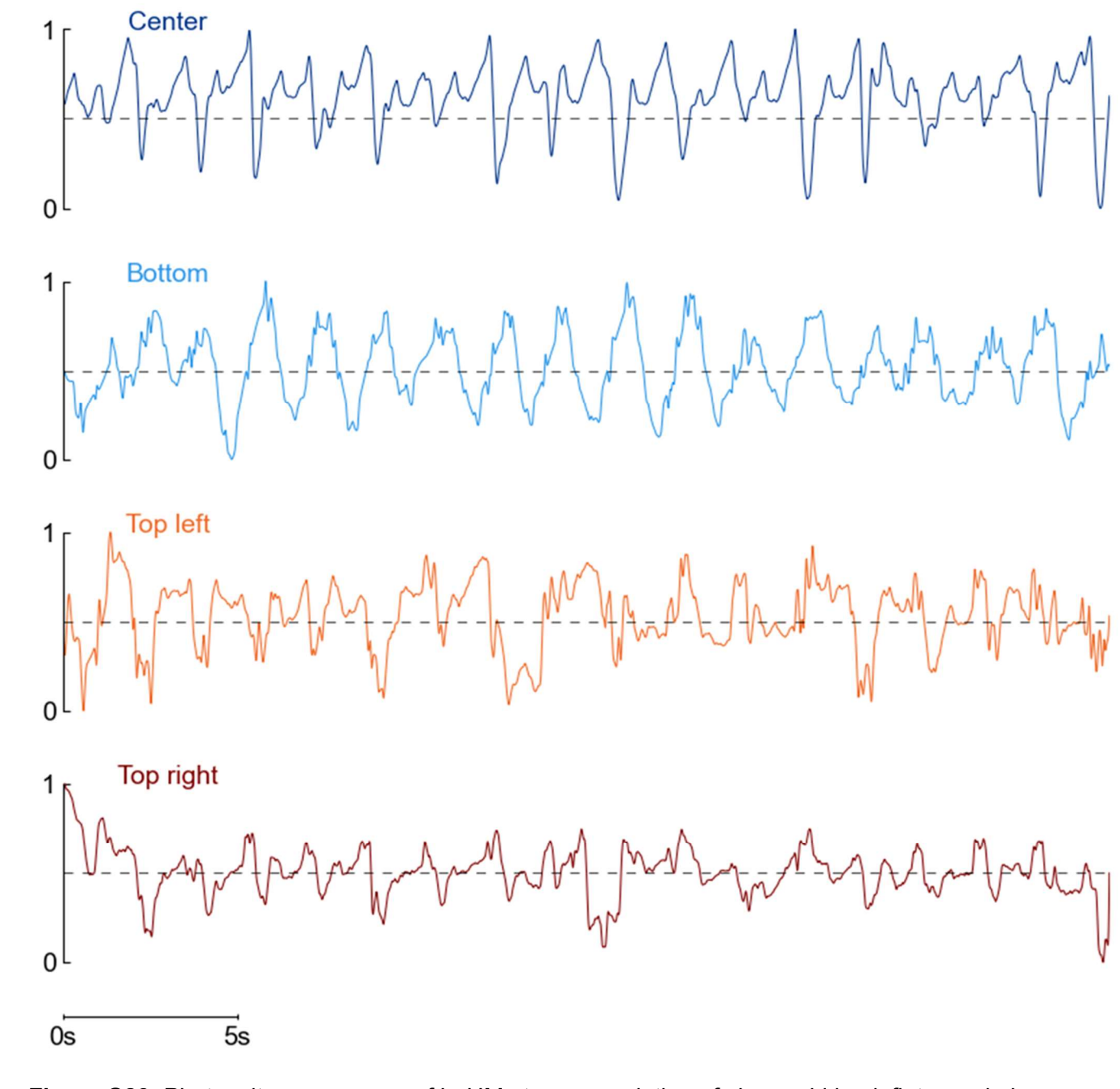
1
2 **Figure S20** Photovoltage response of LaHMo to pronunciation of close back flat vowel phenome.
3



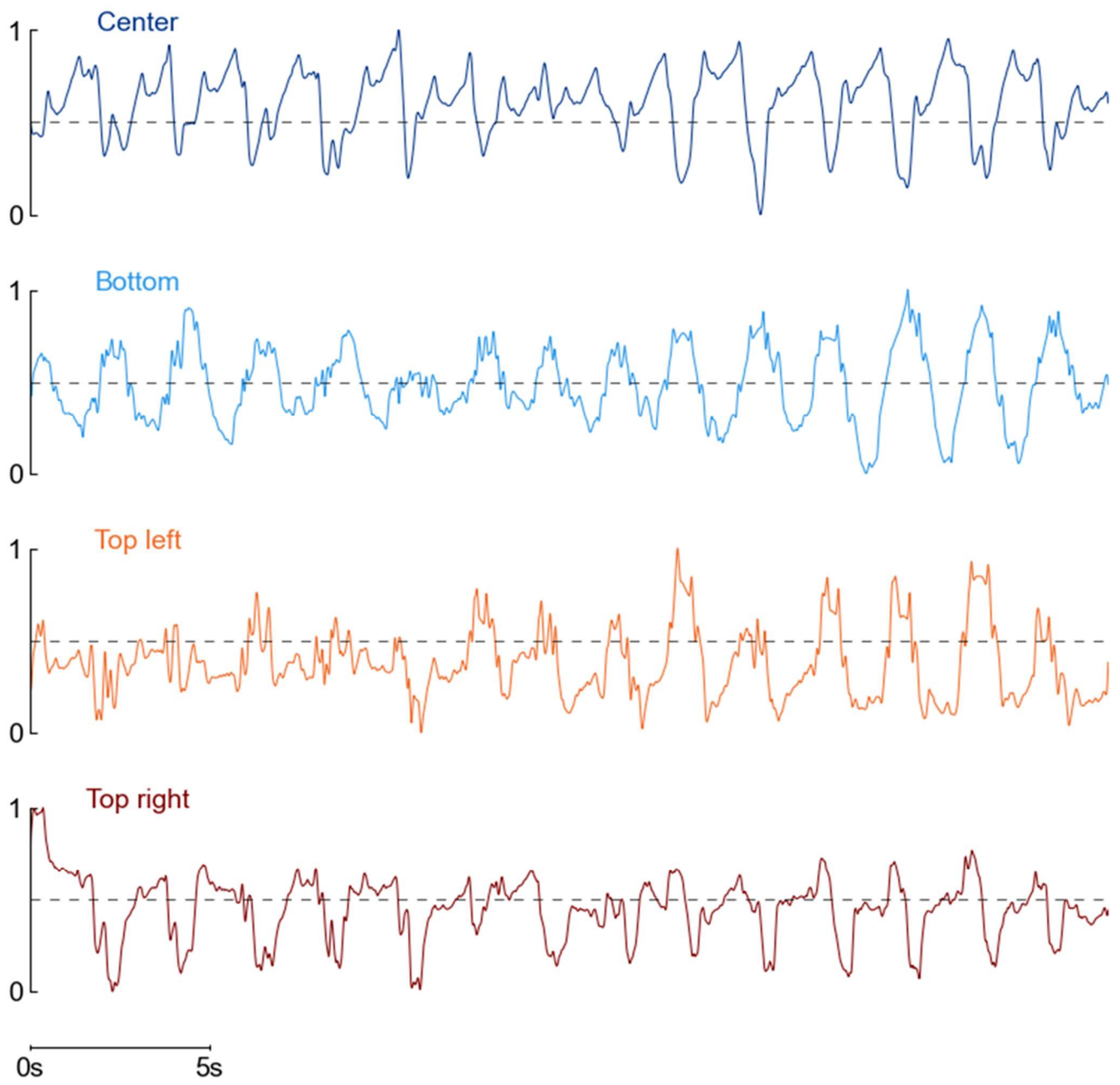
1
2 **Figure S21** Photovoltage response of LaHMo to pronunciation of close central flat vowel phoneme.
3



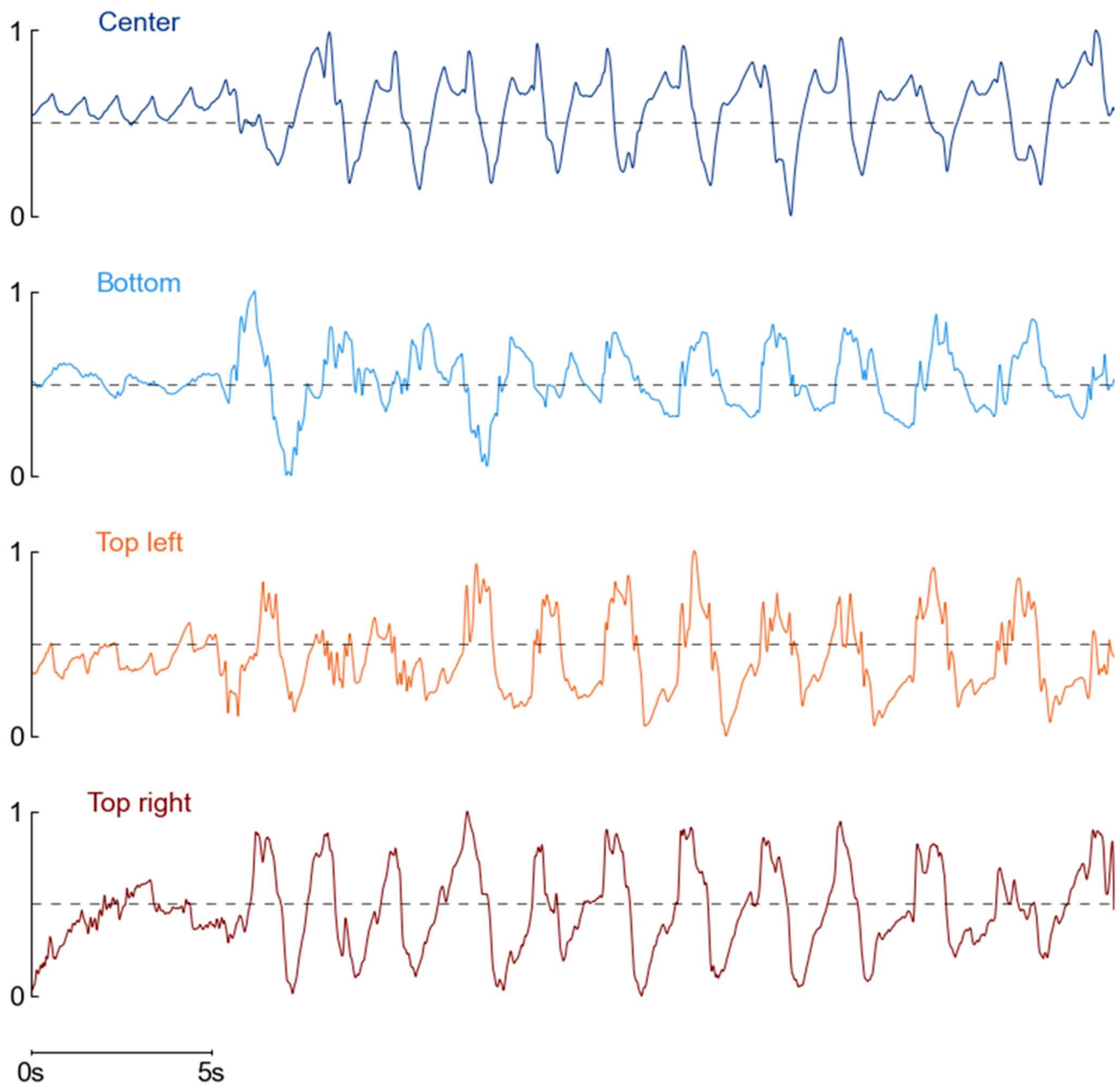
1
2 **Figure S22** Photovoltage response of LaHMo to pronunciation of close front flat vowel phoneme.
3



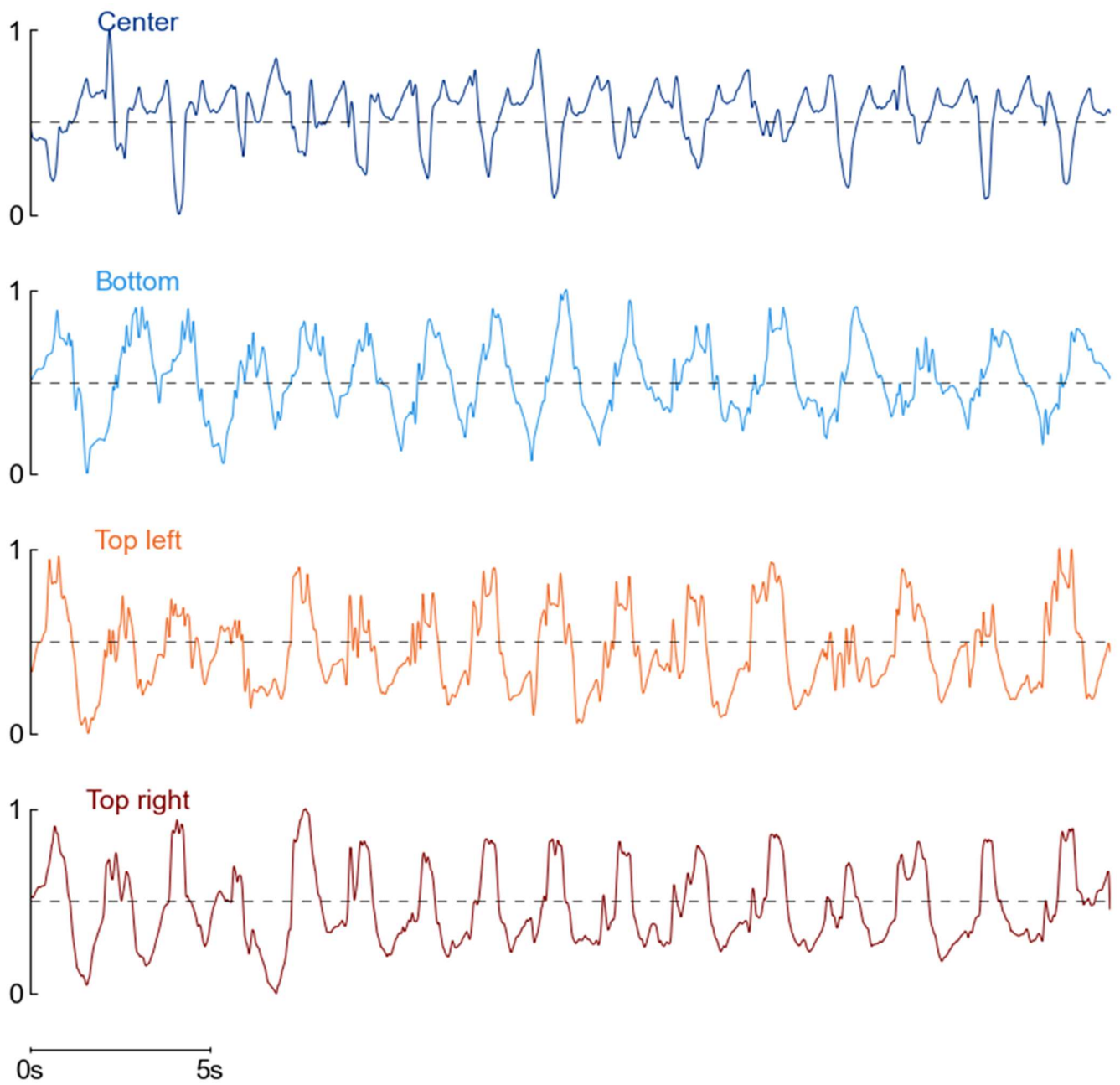
1
2 **Figure S23** Photovoltage response of LaHMo to pronunciation of close-mid back flat vowel phenome.
3



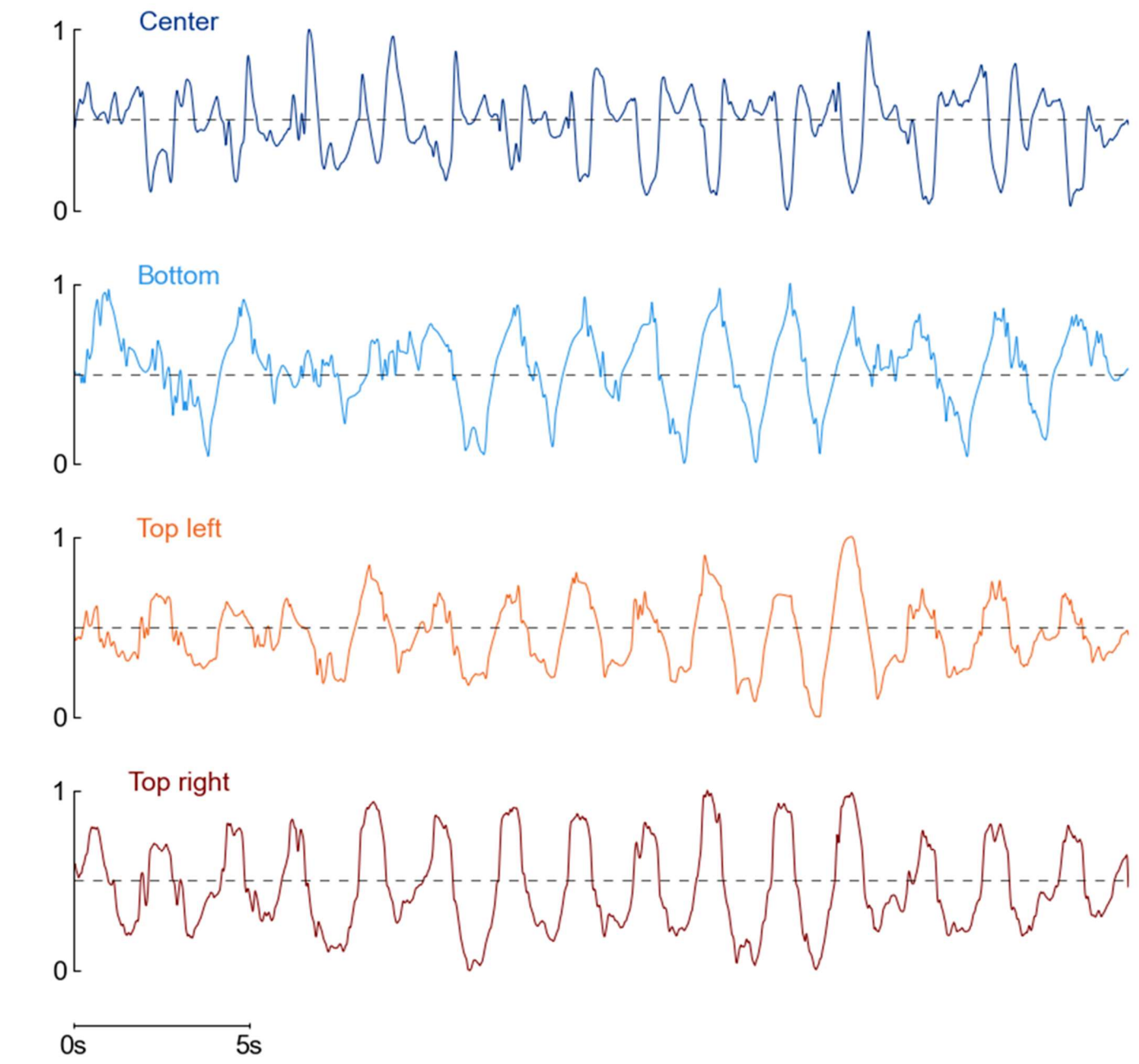
1
2 **Figure S24** Photovoltage response of LaHMo to pronunciation of close-mid central flat vowel
3 phoneme.
4



1
2 **Figure S25** Photovoltage response of LaHMo to pronunciation of close-mid front flat vowel phoneme.
3

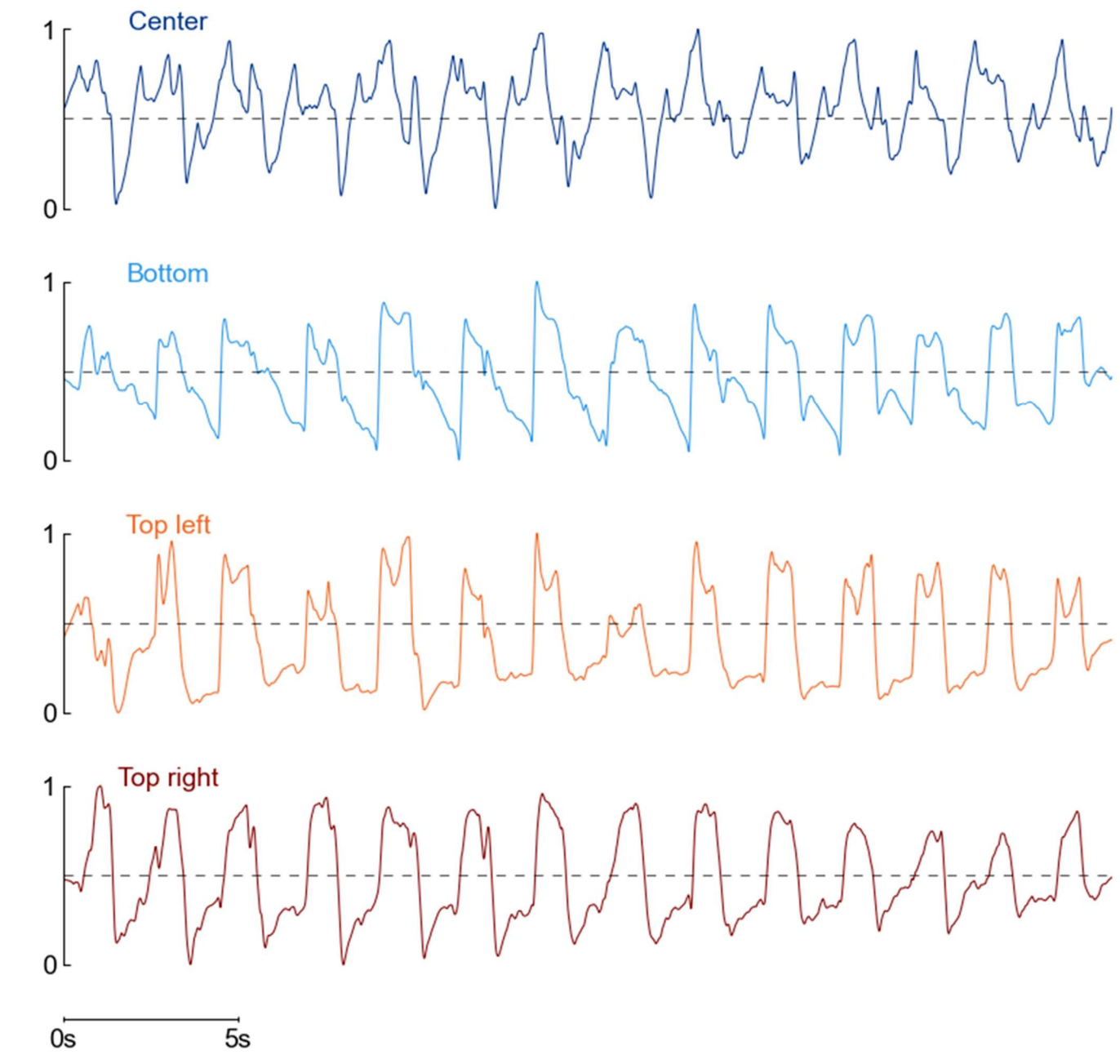


1
2 **Figure S26** Photovoltage response of LaHMo to pronunciation of open-mid back flat vowel phenome.
3



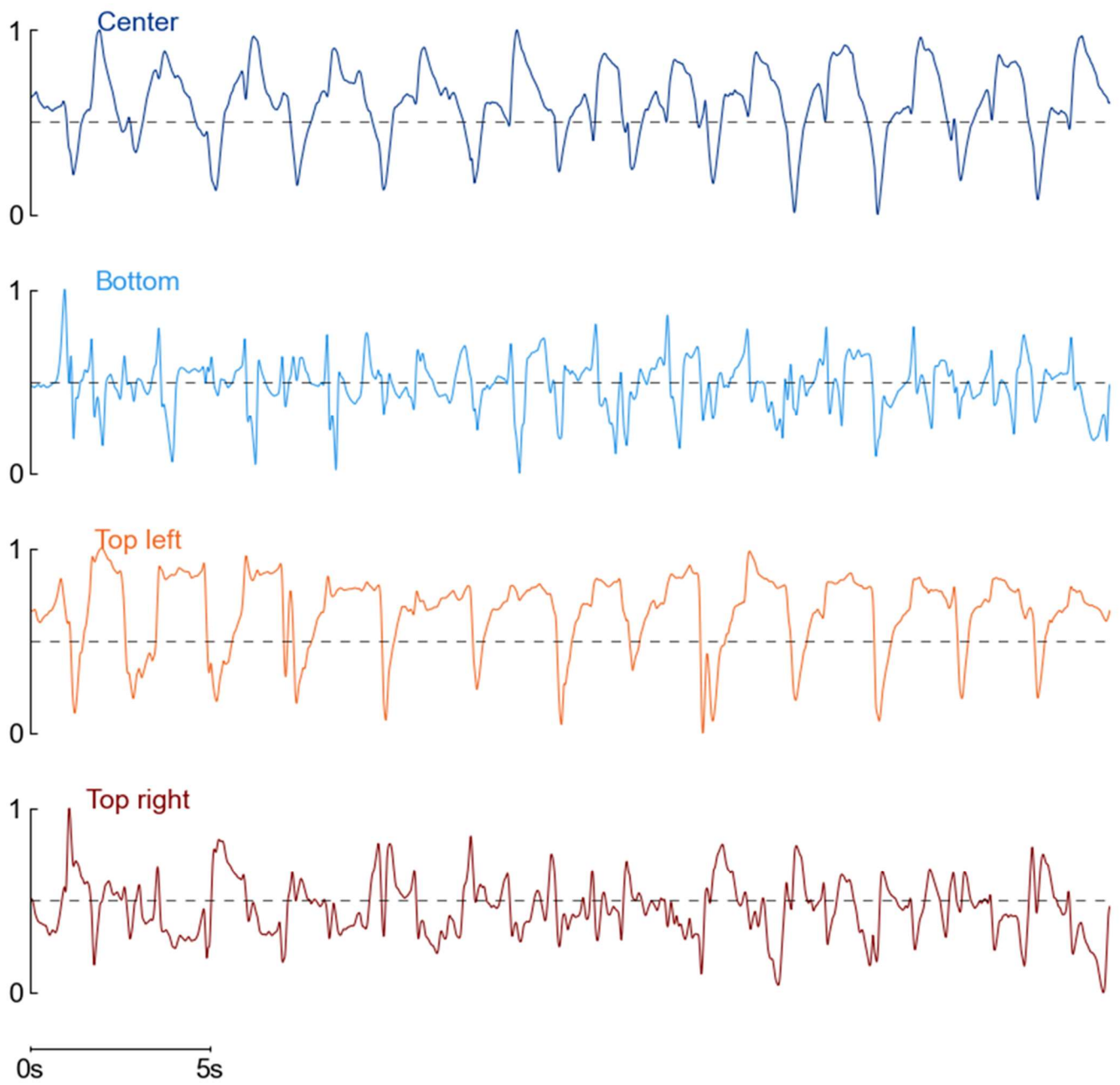
2 **Figure S27** Photovoltage response of LaHMo to pronunciation of open-mid central flat vowel phoneme.

3

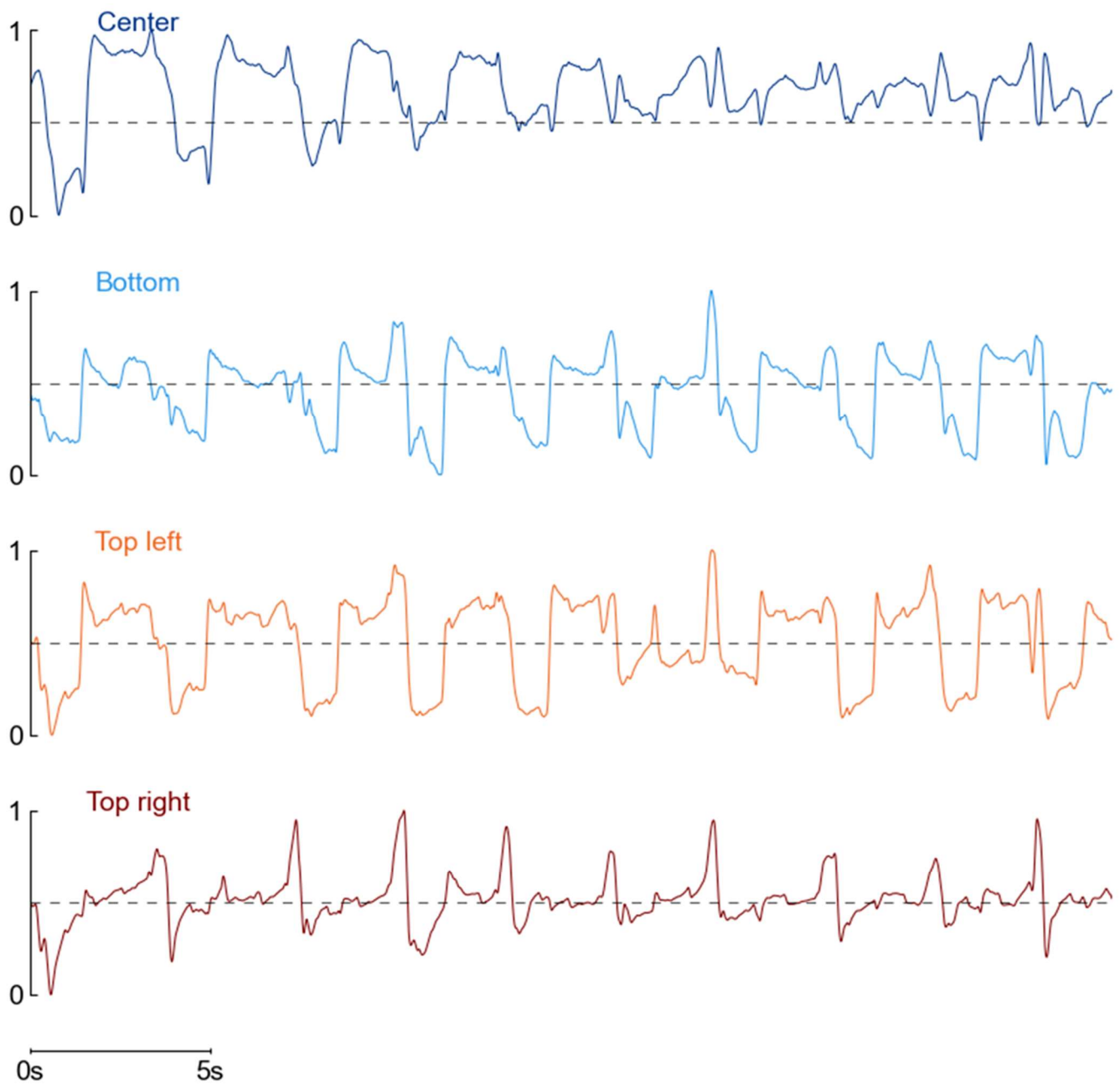


1
2 **Figure S28** Photovoltage response of LaHMo to pronunciation of open-mid front flat vowel phenome.

3



1
2 **Figure S29** Photovoltage response of LaHMo to pronunciation of open back flat vowel phoneme.
3



1
2 **Figure S30** Photovoltage response of LaHMo to pronunciation of open front flat vowel phoneme.
3

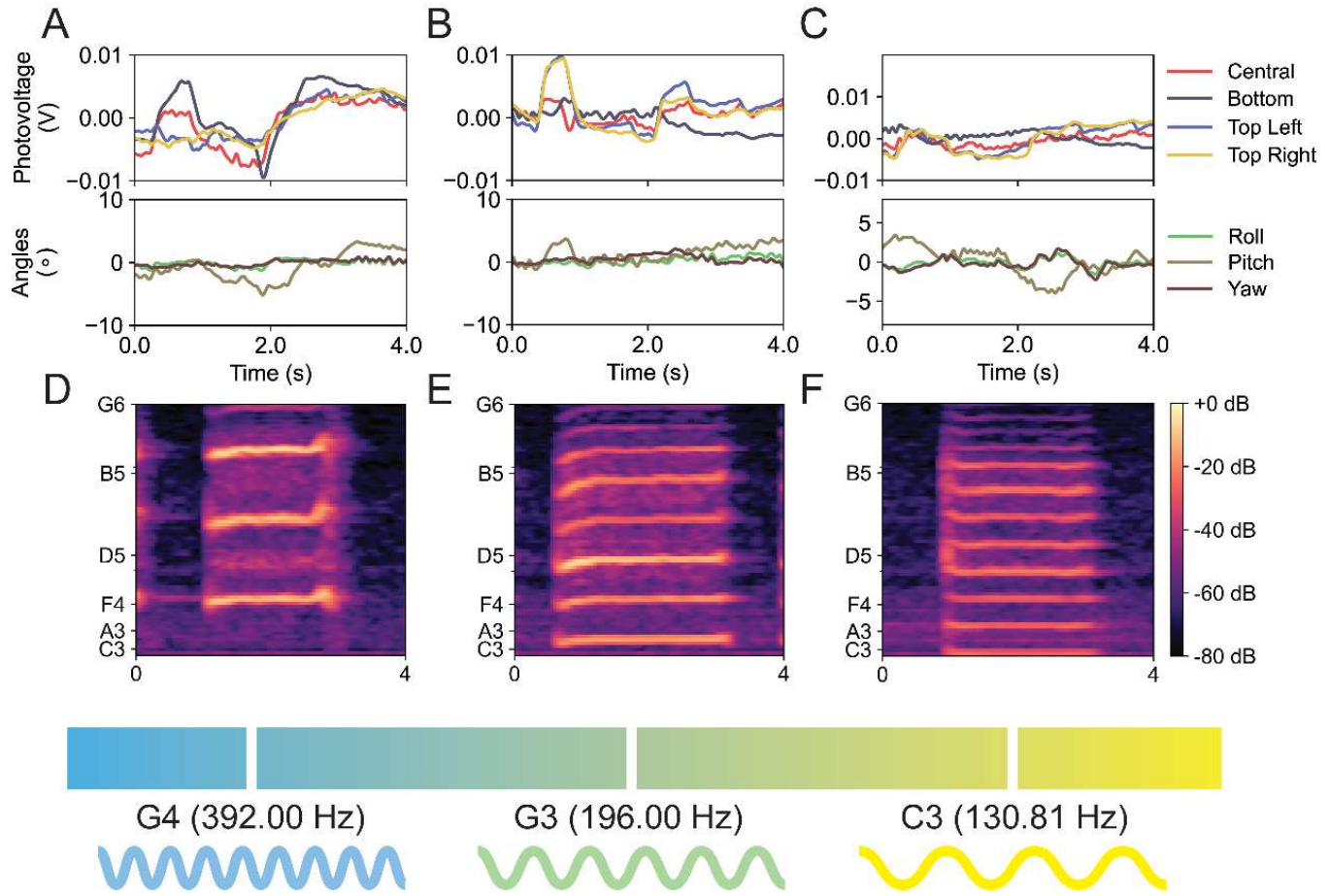
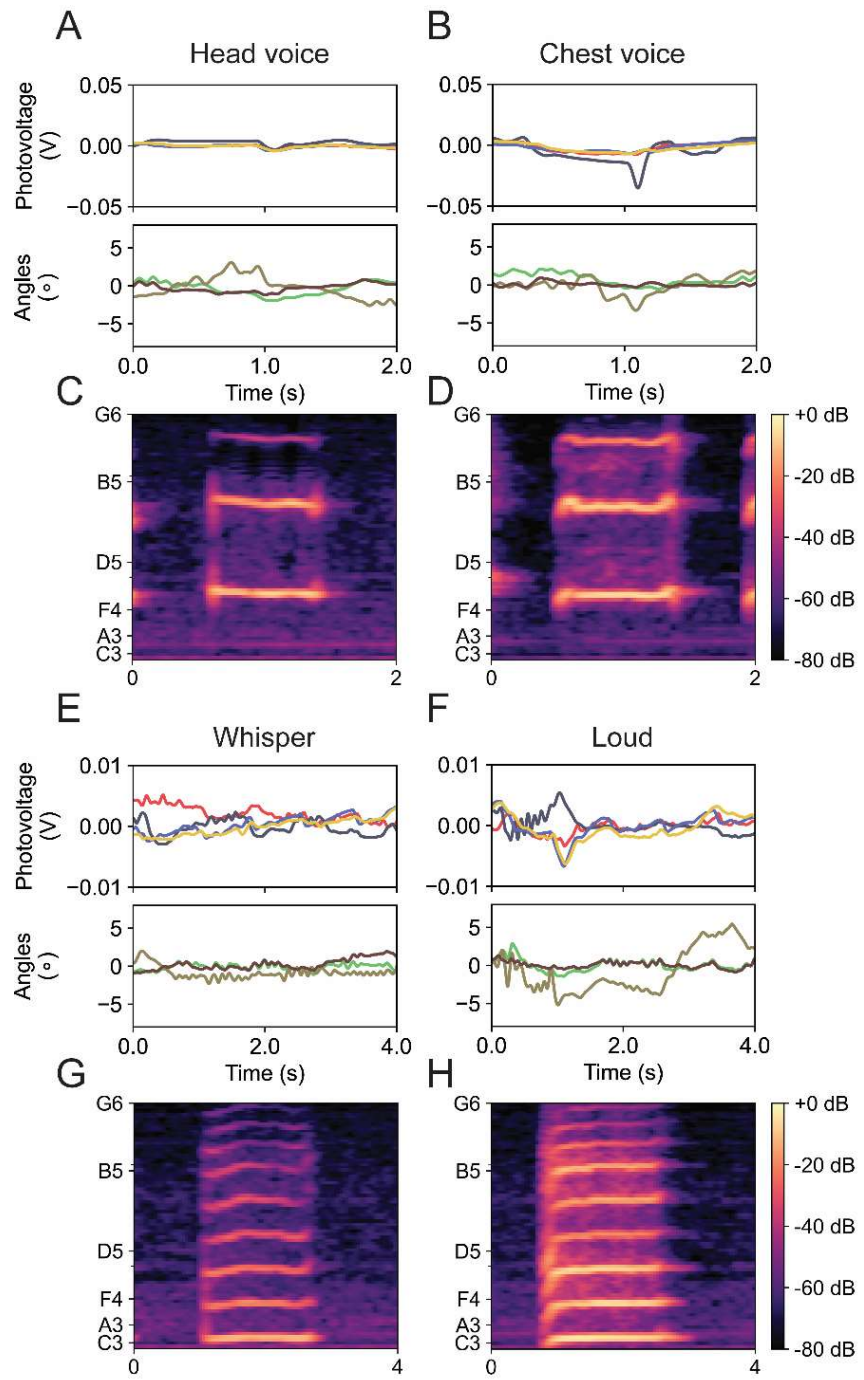
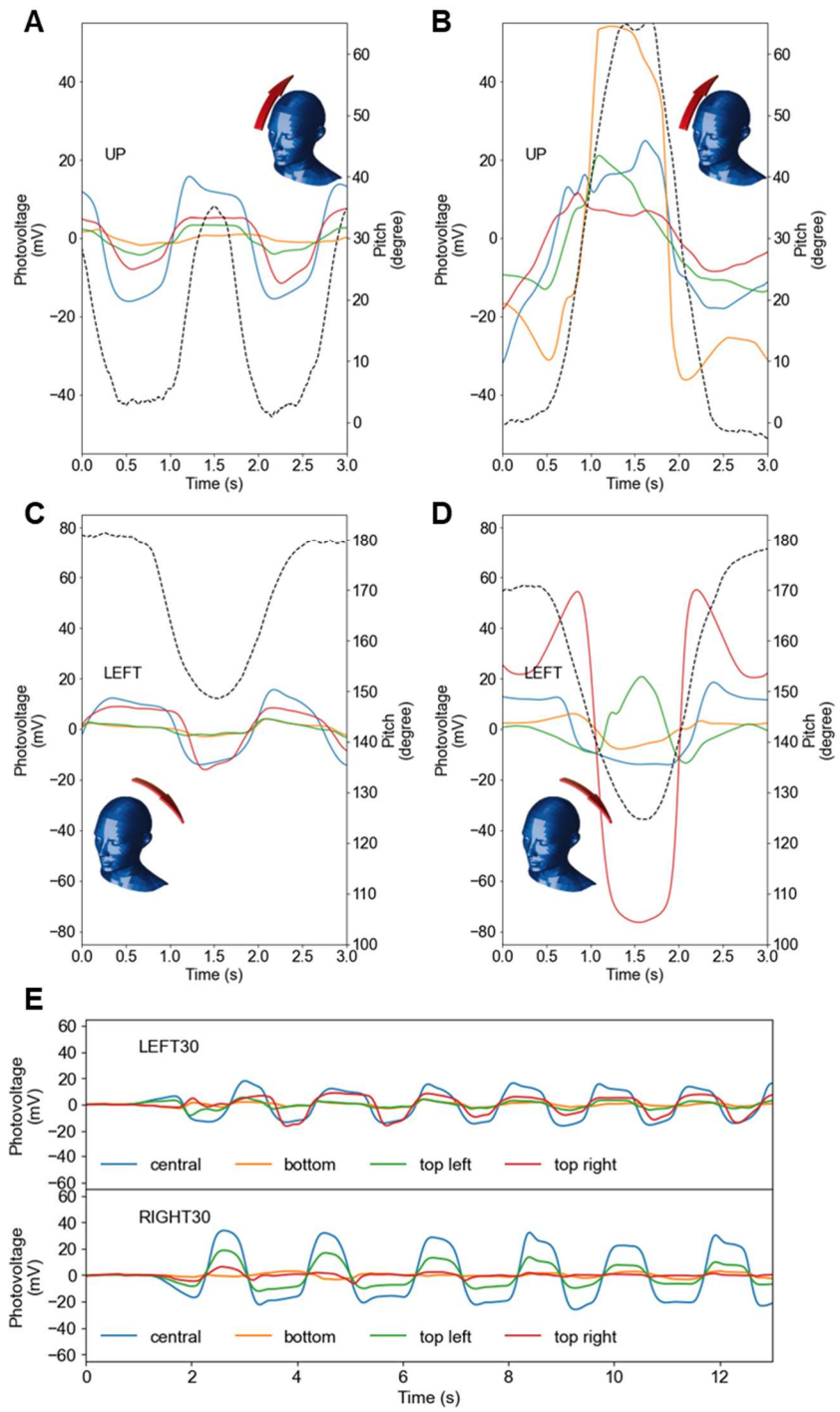


Figure S31(A) The LaHMo data of the subject producing pitch G4. **(B)** The LaHMo data of the subject producing pitch G3. **(C)** The LaHMo data of the subject producing pitch C3. **(D)** The corresponding audio segment of **(A)**. **(E)** The corresponding audio segment of **(B)**. **(F)** The corresponding audio segment of **(C)**.



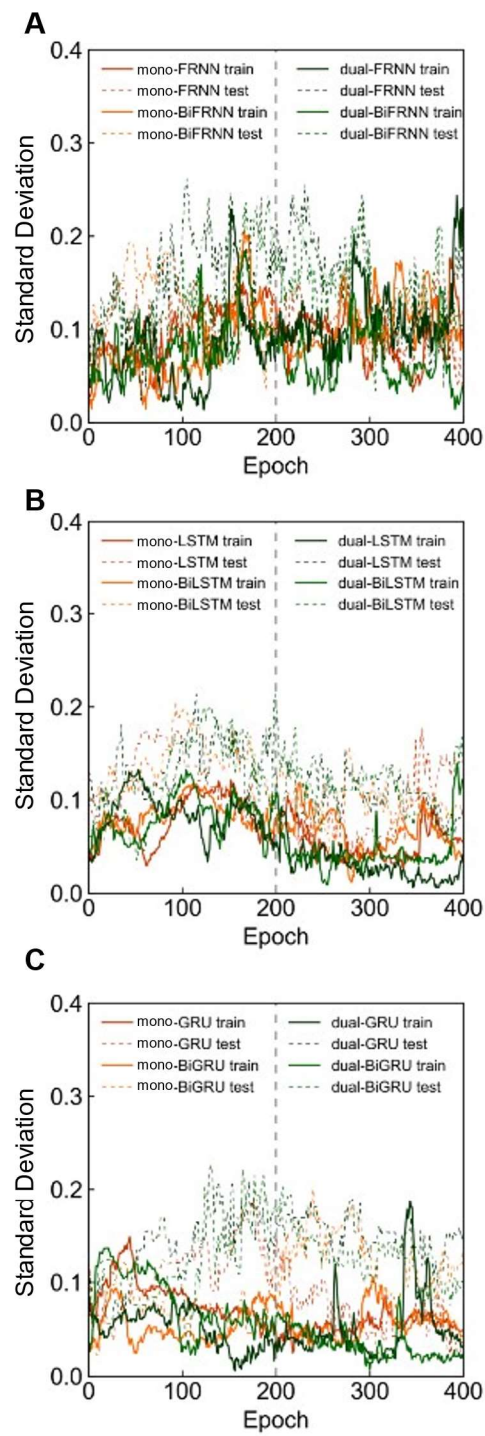
1

2 **Figure S32** (A) The LaHMo data of the subject producing a head voice at pitch G4. (B) The LaHMo
 3 data of the subject produced a chest voice at pitch G4. (C) The corresponding audio segment of (A).
 4 (D) The corresponding audio segment of (B). (E) The LaHMo data of the subject whispers at pitch C3.
 5 (F) The LaHMo data of the subject produces a loud voice at pitch C3. (G) The corresponding audio
 6 segment of (E). (H) The corresponding audio segment of (F).



1

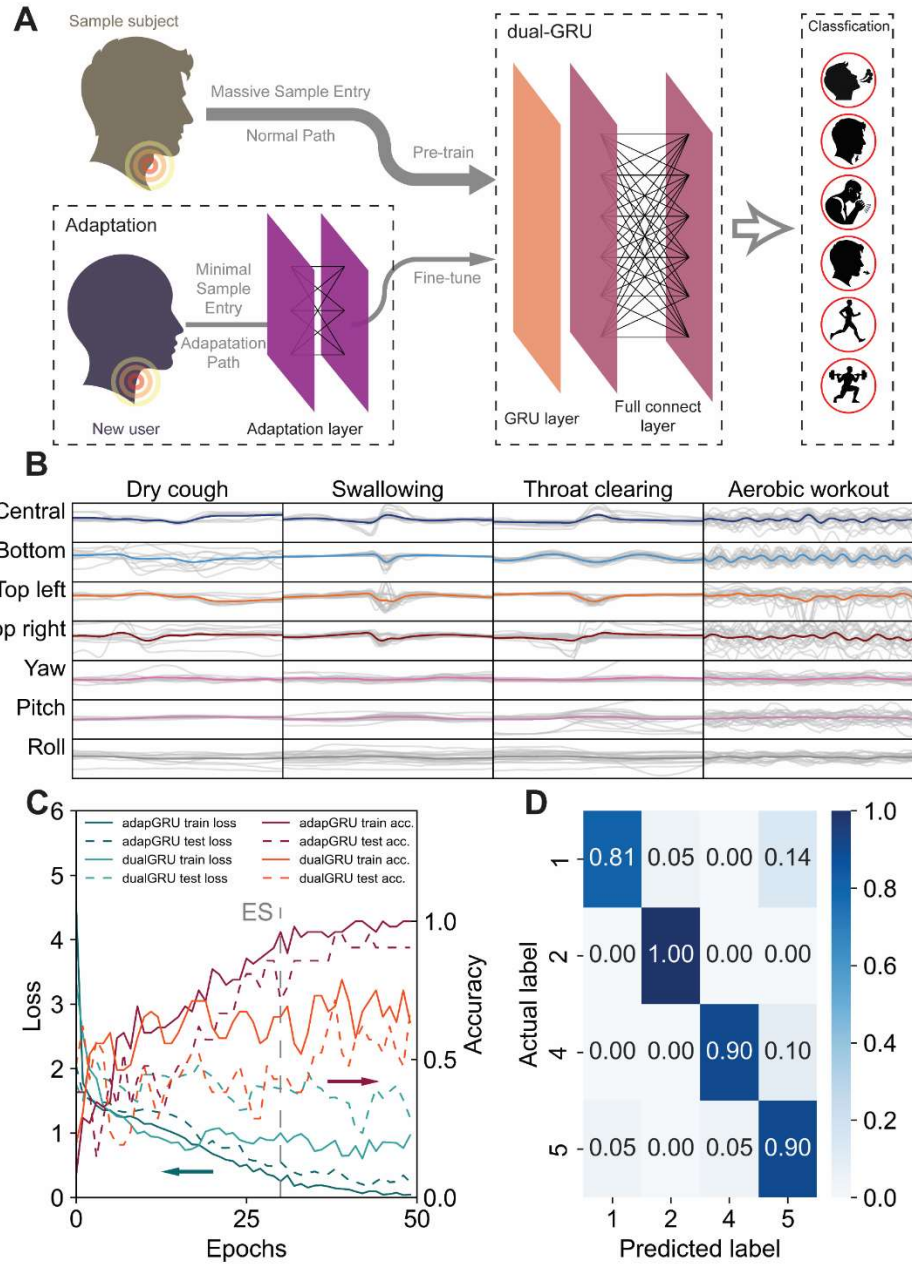
2 **Figure S33** Comparison of the photodiode response of LaHMo to different head motions. (A) Cervical
 3 extension, 30 degrees. (B) Cervical extension, 60 degrees. (C) Cervical left bending, 15 degrees. (D)
 4 Cervical left bending, 30 degrees. (E) Continuous response to left and right bending, 30 degrees. Color
 5 labels: Blue: center; Orange: bottom; Green: top left; Red: top right; Black dashed: ground truth value
 6 collected by IMU.



1

2 **Figure S34** Training and testing standard variation during model training process when doing a k-fold
3 cross validation. (A) mono- and dual-FRNN. (B) mono- and dual-LSTM. (C) mono- and dual-GRU.

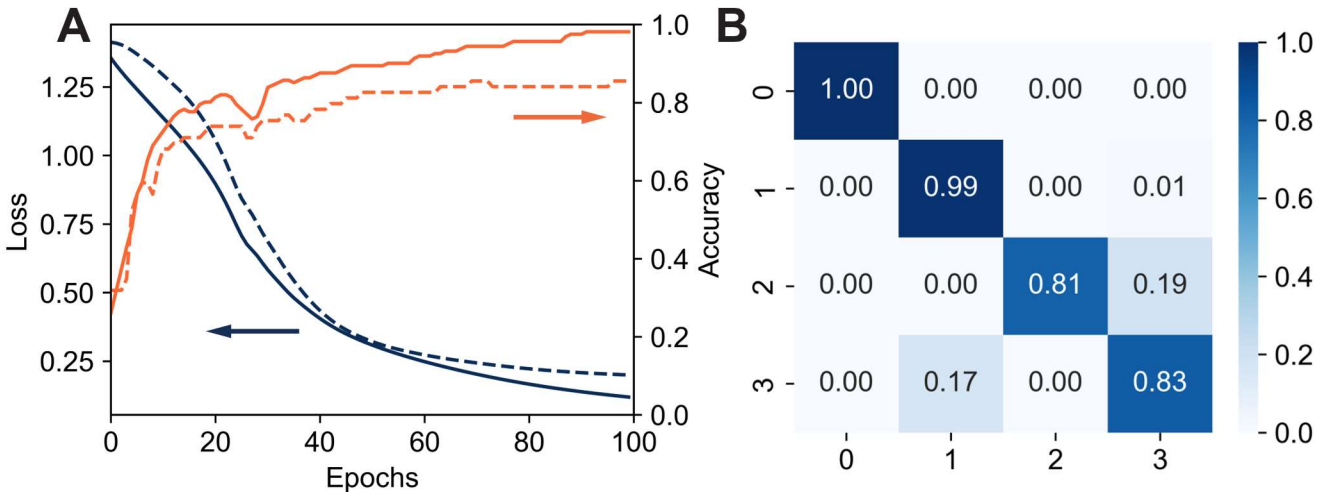
4



1

2 **Figure S35. Domain adaptation to facilitate individualization of AI analysis.** (A) Training-process
3 visualization of the domain-adaptation network (adap-GRU). (B) Graphical representation of the four
4 inputs required to train the adap-GRU. Photovoltage and Euler angle data over the course of the four
5 physiological activities of interest are displayed, with gray lines representing raw data from tests and
6 the colored lines presenting the averages. (C) The accuracy and loss curves of training and testing for
7 the dual- and adap-GRU models. The results show that the adap-GRU network (96.1% accuracy at ES
8 = 30 epochs) can be trained significantly faster than a brand-new dual-GRU network (65.4% accuracy
9 at ES = 30 epochs). (D) The confusion matrix of the test data shows the algorithm prediction of the
10 event type and the actual event type (1-swallowing, 2-dry cough, 4-throat clearing, 5-aerobic workout).

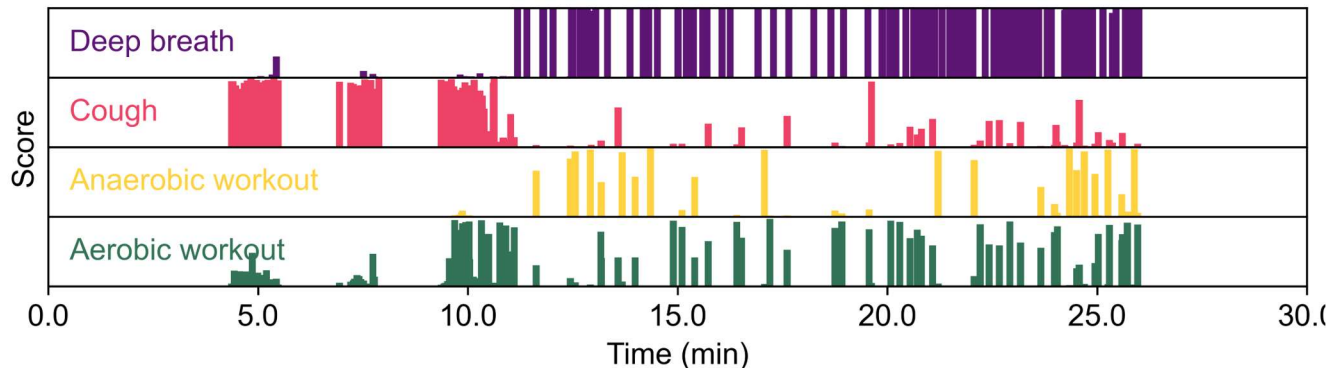
11



1

2 **Figure S36** (A) the accuracy and loss curves for the model's training (solid) and testing (dashed), with
 3 the model shown to become increasingly accurate and confident in predicting physiological events as
 4 the test progressed over 100 epochs. (B) The confusion matrix of the model's predictions of activity
 5 compared to the actual activities, further showing the model's efficacy over the experiment. It reports
 6 event identification accuracies of 1.00 for deep breaths, 0.99 for dry coughs, 0.81 for anaerobic
 7 workouts, and 0.83 for aerobic workouts, labeled from 0 through 3, respectively.

8



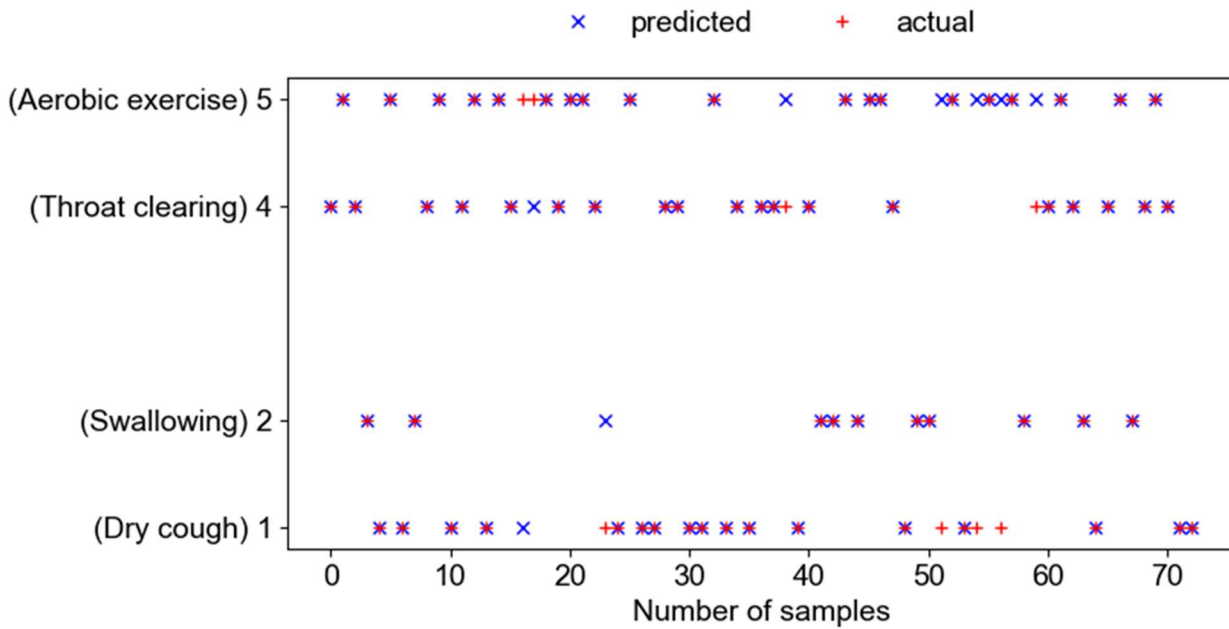
1

2 **Figure S37** Within each vertical space are purple, red, yellow, and green pillars representing the
 3 possibility of the model classifying the event as a deep breath, cough, anaerobic workout motion,
 4 and aerobic workout motion, respectively. A higher pillar shows a higher score on the corresponding label.
 5 For each 3-second slice that the preprocessor decides that a feature occurs, the model will attempt to
 6 identify the current action by computing the score for each label. If the score for a certain label is the
 7 most significant among all the other labels and is over 0.6, a prediction will be made. If the maximum
 8 score for a given 3-second slice is below 0.6, the model will terminate the attempt and output as an
 9 “unknown” label.

10

1

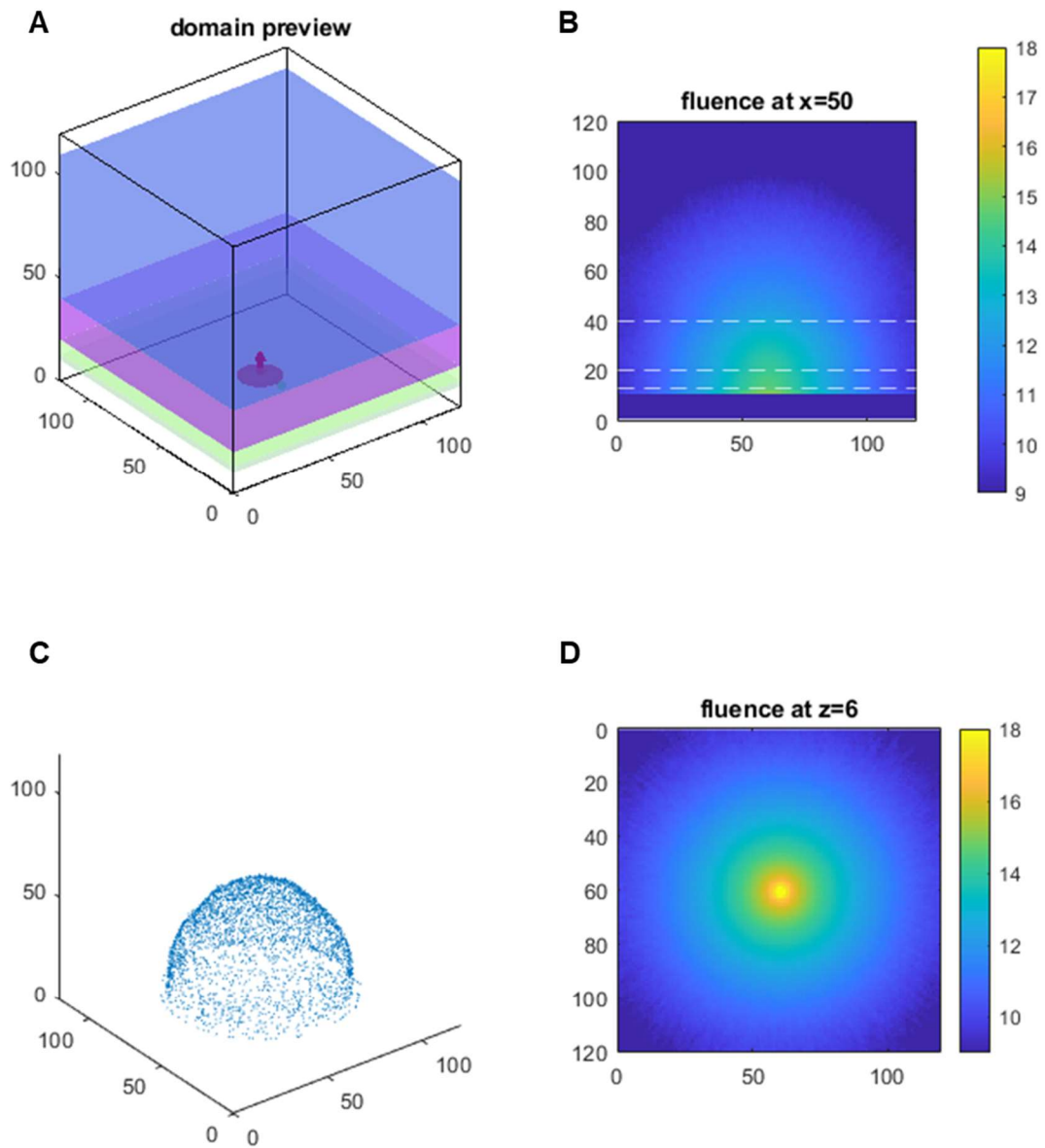
2



3

4 Figure S38 Prediction of adap-GRU on target user.

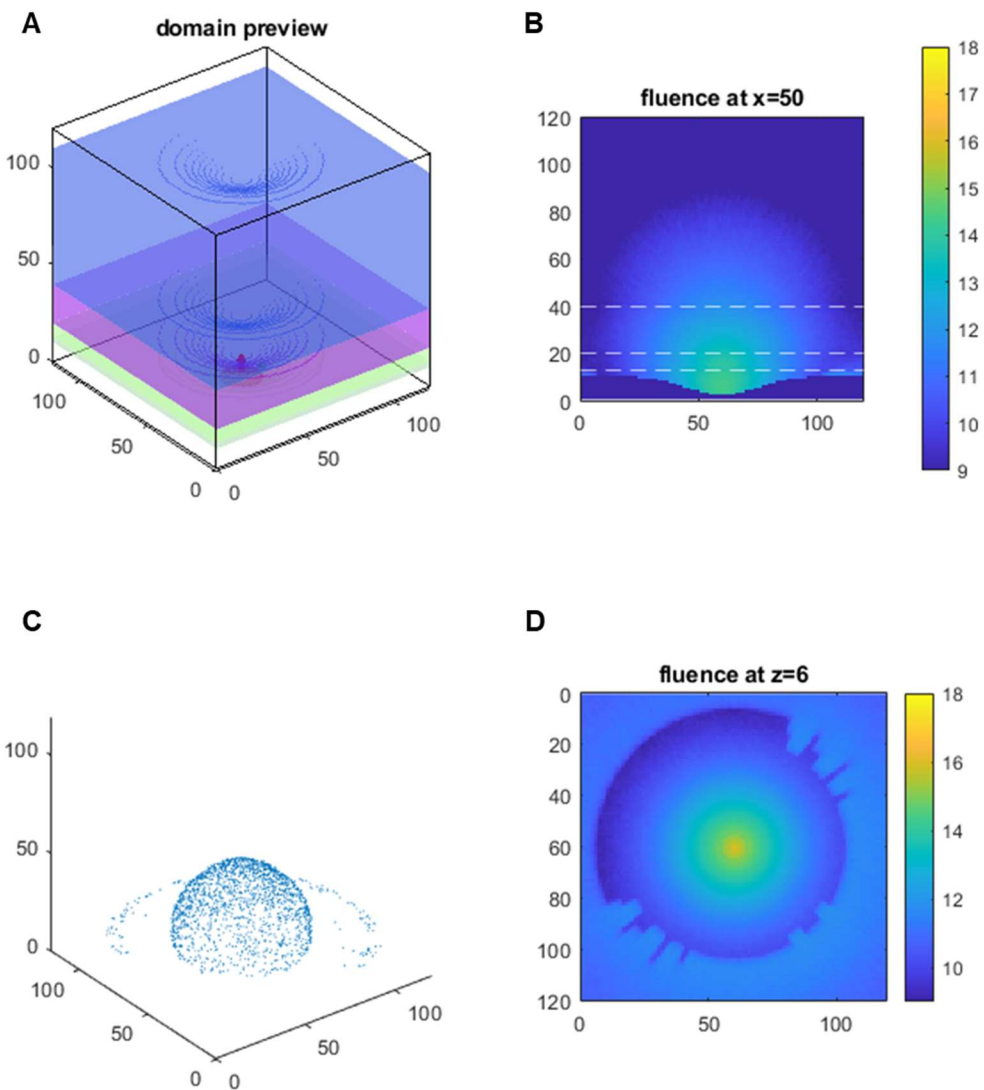
5



1

2 **Figure S39** Basic Monte Carlo simulation of the patch applied on a tissue surface. (A) Model setup.
 3 Yellow: epidermis. Green: dermis. Purple: subcutaneous fatty tissue. Blue: muscle. Red circle and
 4 arrow: location and direction of the light source. Green circle: location and size of the photodetector. (B)
 5 Vertical cross-section fluence profile at the light source. (C) Highlighted spatial elements with fluence
 6 1/100 of the light source. (D) Horizontal cross-section fluence profile at the interface of epidermis and
 7 background.

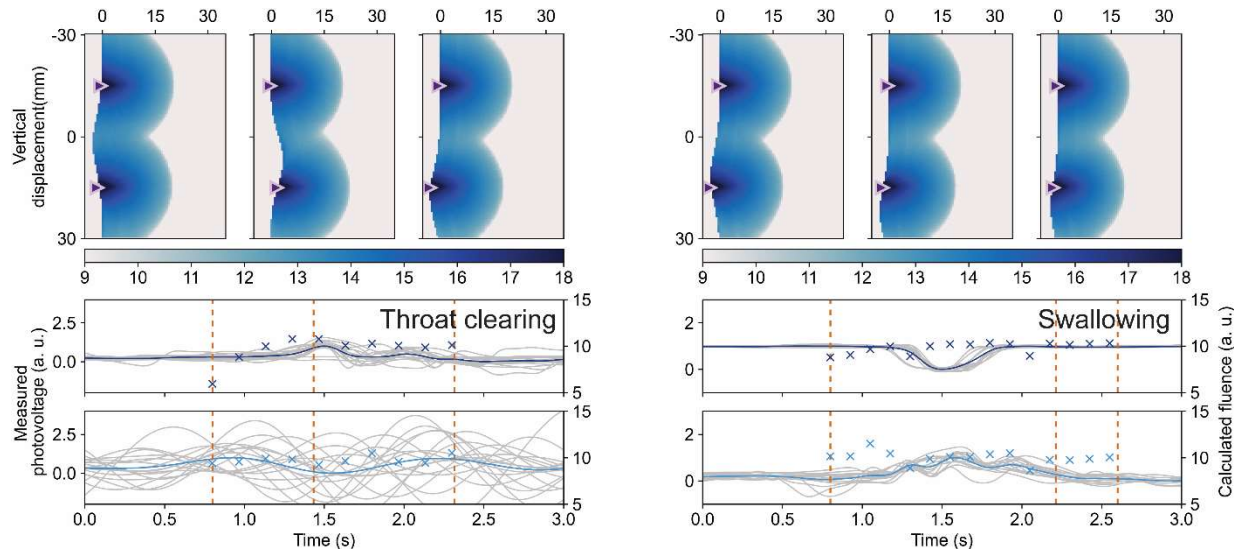
8



1

2 **Figure S40** Basic Monte Carlo simulation of the patch applied on a laryngeal prominence. (A) Model
 3 setup. Yellow: epidermis. Green: dermis. Purple: subcutaneous fatty tissue. Blue: muscle. (B) Vertical
 4 cross-section fluence profile at the light source. Red circle and arrow: location and direction of the light
 5 source. Green circle: location and size of the photodetector. (C) Highlighted spatial elements with
 6 fluence 1/100 of the light source. (D) Horizontal cross-section fluence profile at the interface of
 7 epidermis and background.

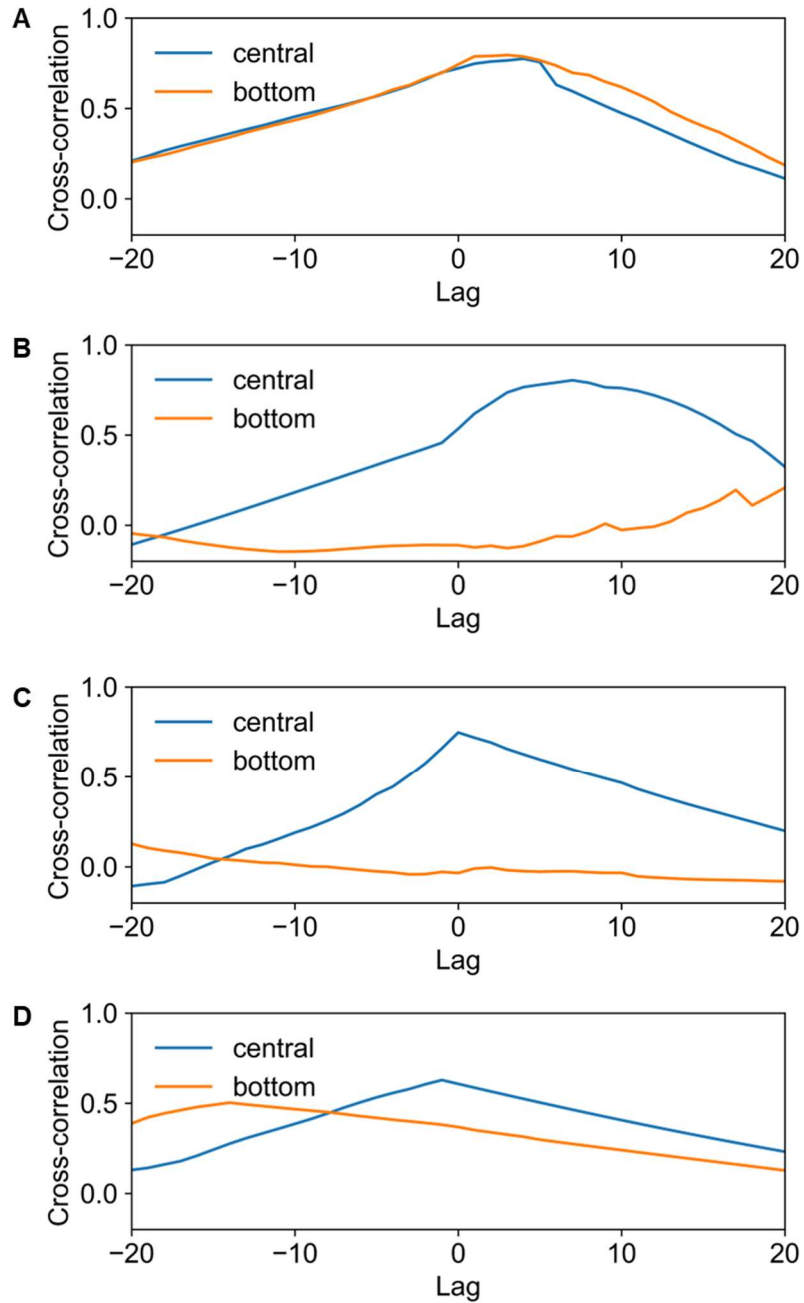
8



1 **Figure S41** Simulation results on the cross-sectional profiles of LED illumination from a LaHMo patch
2 into the neck and their accompanying measured photovoltage and calculated fluence data during the
3 throat clearing and swallowing events.
4
5

6

1



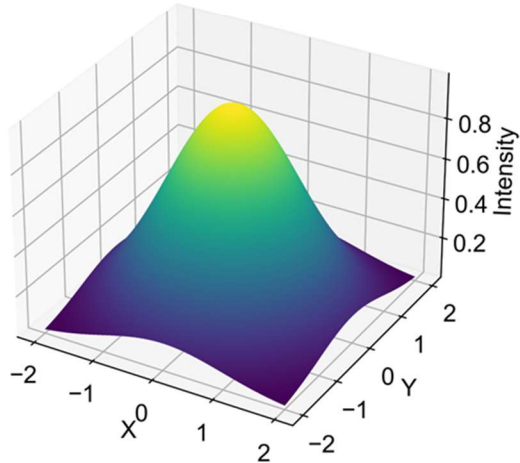
2

3 **Figure S42** Cross-correlation between MC simulation results and NIRS measurements for (A) deep
4 breath, (B) dry cough, (C) throat clearing, and (D) swallowing.

5

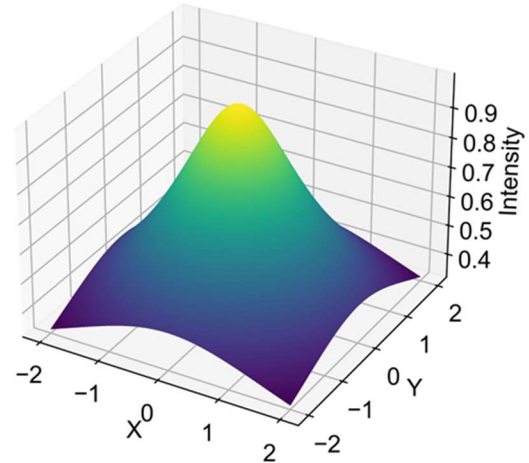
A

Two-Element Gaussian Distribution



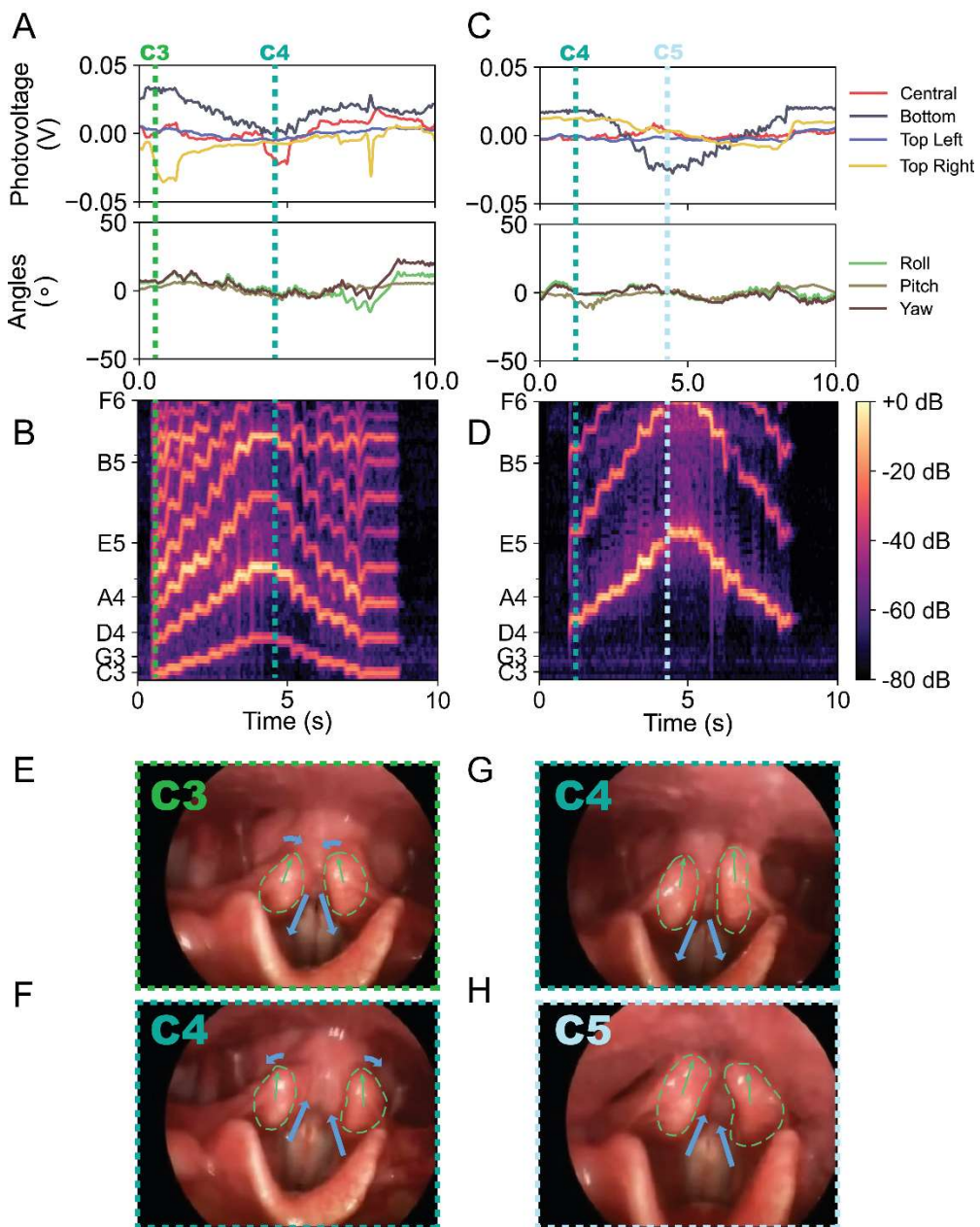
B

Lambertian Distribution



1

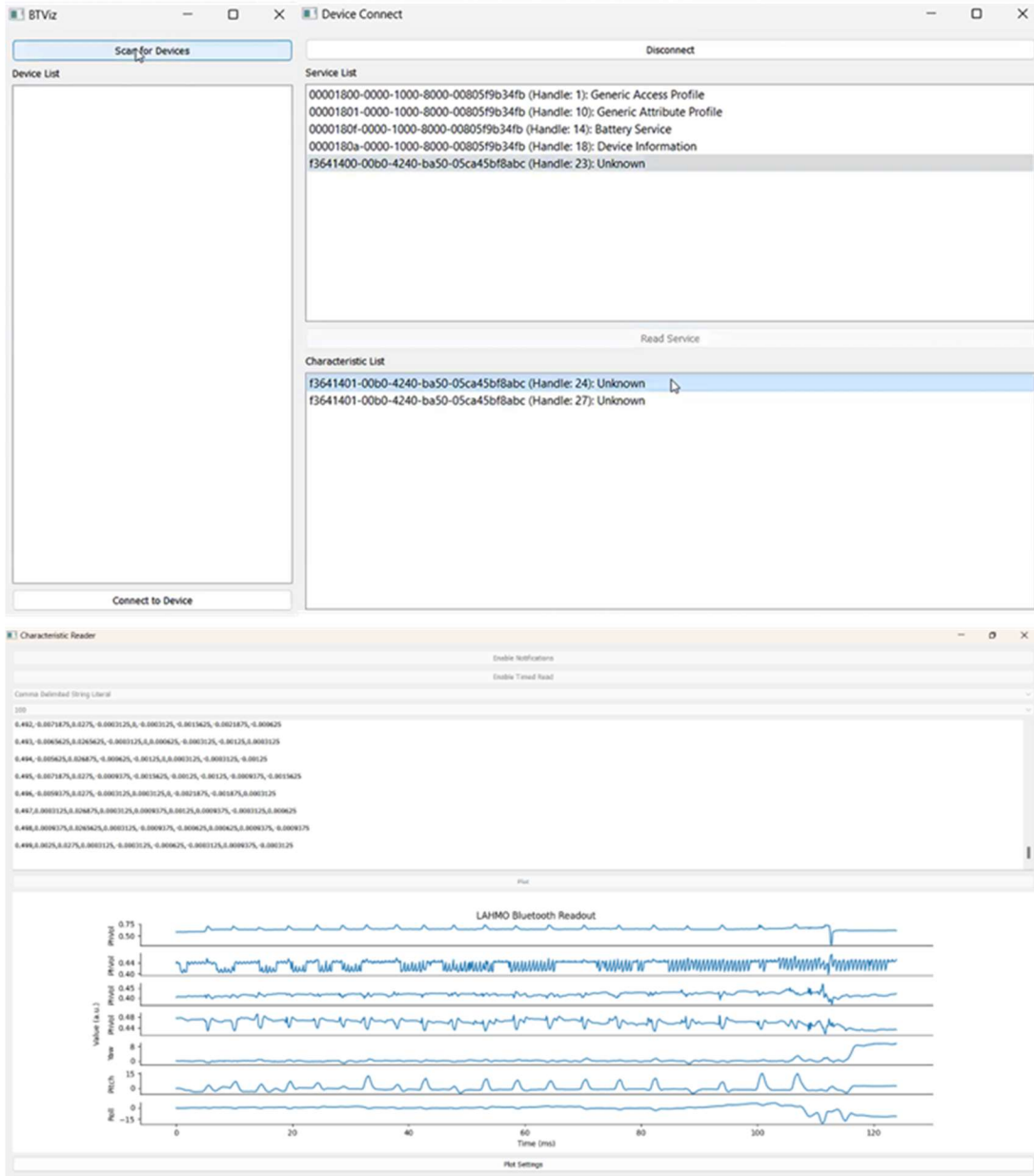
2 **Figure S43** The comparison between a (A) two-element Gaussian distribution and (B) Lambertian
3 distribution in the range from -2 to 2. The Gaussian distribution uses a standard deviation of 1 for both x
4 and y variables.



1

2 **Figure S44** (A) LaHMo data of the subject producing a cycle of natural musical scale from C3 to C4,
3 and back to C3, using chest voice. (B) The corresponding audio recording of the test segment
4 presented in (A). (C) LaHMo data of the subject producing a cycle of natural musical scale from C4 to
5 C5, and back to C4, using falsetto. (D) The corresponding audio recording of the test segment
6 presented in (C). The green and aqua dashed lines represent the C3 and C4 note samples that
7 correspond to the videostroboscopy slices in (E-H). (E) Videostroboscopy slice at chest voice C3. (F)
8 Videostroboscopy slice at chest voice C4. (G) Videostroboscopy slice at falsetto voice C4. (H)
9 Videostroboscopy slice at falsetto voice C5. Green dashed circles in (E-H) highlight the corniculate
10 cartilages, green arrows label the central line of the cross-section of the corniculate cartilages, pointing
11 at anterior. Blue arrows highlight the moving trend of the corniculate cartilage in order for the subject to
12 produce the corresponding note.

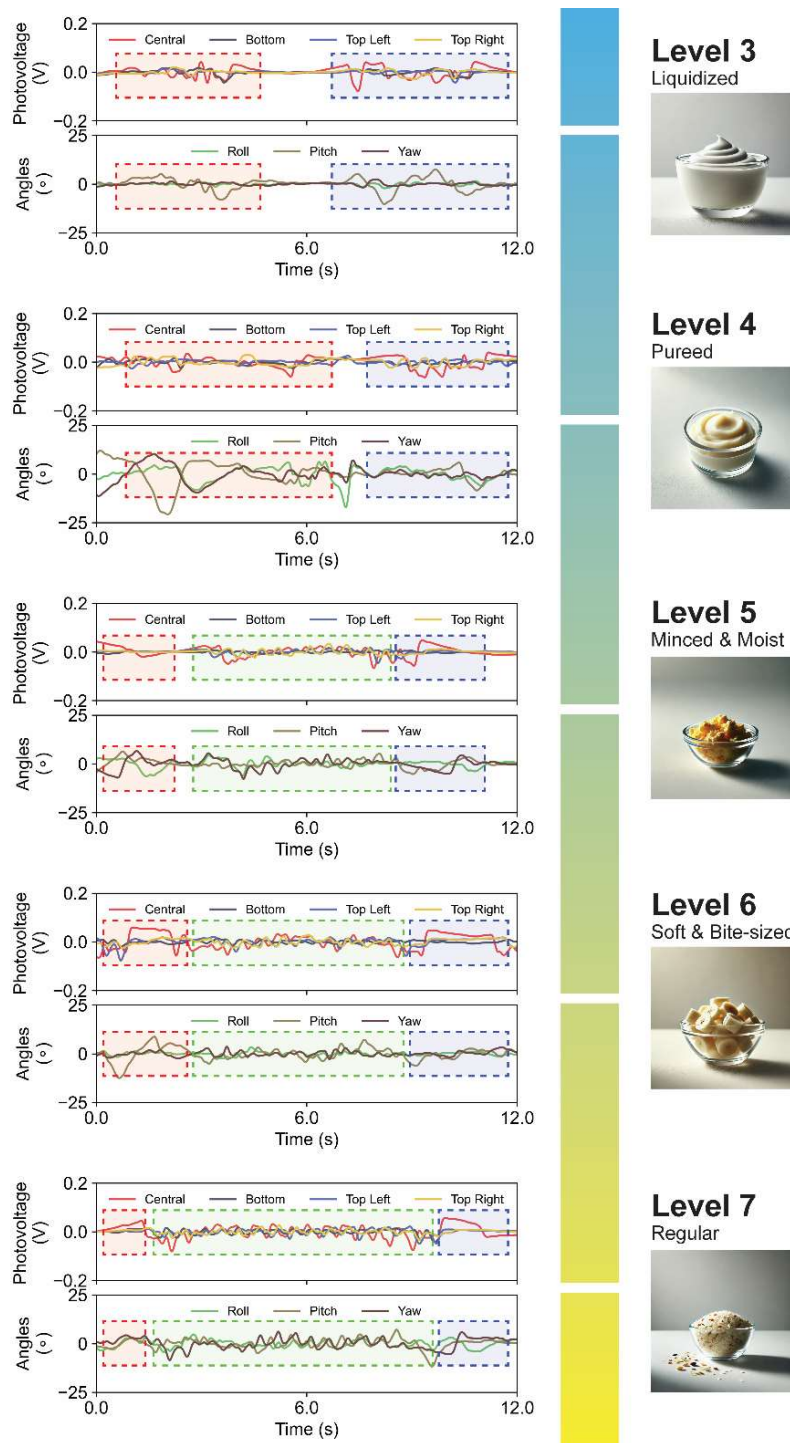
1
2
3



4

5 **Figure S45** The graphic interface of the BTviz. The top left panel shows the device scanning widget,
6 used to connect to the specified device. The top right panel shows the service/characteristic selection
7 widget. The bottom panel shows the characteristic reader that decodes the received BLE data and
8 implements the real-time visualization.

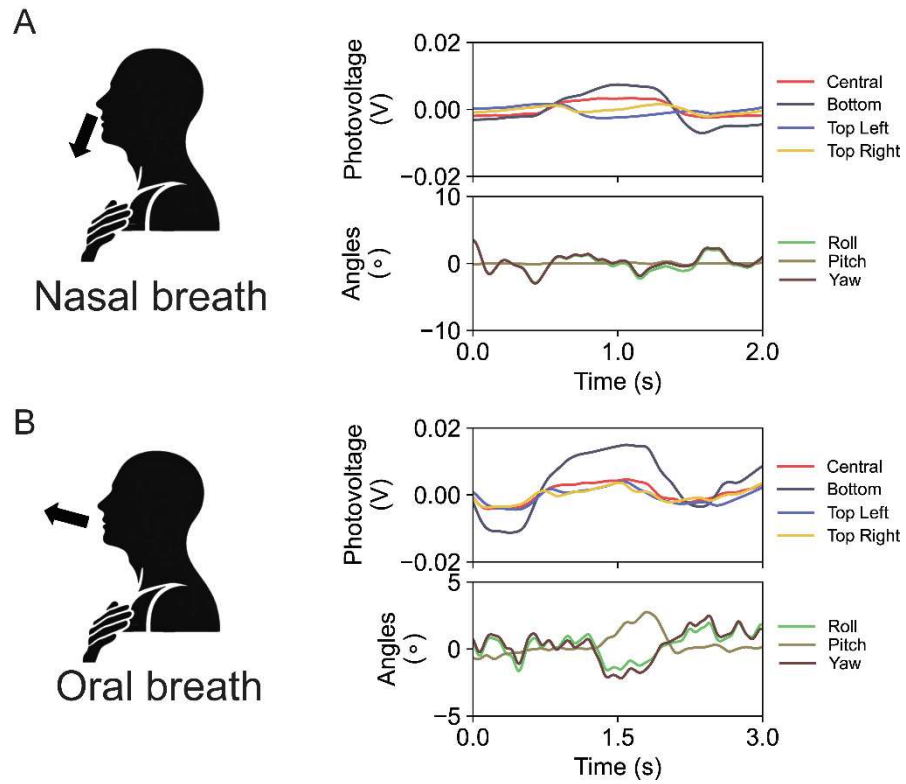
9



1

2 **Figure S46** LaHMo data of solid food bolus with an increasing viscosity from top to bottom. The left
 3 column shows the example of the acquired signal at different viscosity levels, and the right column
 4 shows a food example for each viscosity level.

5



1

2 **Figure S47** (A) The LaHMo data segment presenting a nasal breath attempt. (B) The LaHMo data
3 segment presenting an oral breath attempt.

4

1 **Movie**

2 **Movie S1 On-body testing of LaHMo system.** The left panel shows a synchronized video of the test
3 subject performing the physiological actions of interest under the direction of the investigators. The top
4 middle panel shows the live responses of the photovoltages (darkness of the T-shape) and the Euler
5 angles (orientation of the T-shape). The color of the pixels on the T-shape is interpolated from the
6 measurements of the four PDs. The orientation of the three rings are the results of the Madgwick filter
7 with the input from the IMU. The bottom middle panel shows the screen recording of the LaHMo data
8 recording interface, showing the seven live data collections. The right panel shows the data replay of
9 the whole experiment, with the progressing bar on the top showing the real-time activity being tested.

10 **Movie S2 Computational analysis of correlation between LaHMo signals and corresponding**

11 **muscular movements from neck.** Closeup footage of four physiological actions of interest (deep
12 breath, dry cough, throat clearing, and swallowing) in the laryngeal region with the corresponding
13 fluences of NIR light emitted from the central and bottom LEDs. The top left panel shows the live
14 fluence mapping of the corresponding activity on the sagittal cross-section of the laryngeal prominence.
15 The bottom left panel shows live fluence mapping of the corresponding activity the coronal cross-
16 section of the laryngeal prominence.

1 **References**

- 2 1. Madgwick, S. An efficient orientation filter for inertial and inertial/magnetic sensor arrays. *Report
3 x-io and University of Bristol (UK)* (2010).
- 4 2. Fang, Q. & Boas, D. A. Monte Carlo Simulation of Photon Migration in 3D Turbid Media
5 Accelerated by Graphics Processing Units. *Optics Express* **17**, 20178–20190 (2009).
- 6 3. Simpson, C. R., Kohl, M., Essenpreis, M. & Cope, M. Near-infrared optical properties of ex vivo
7 human skin and subcutaneous tissues measured using the Monte Carlo inversion technique.
8 *Phys Med Biol* **43**, 2465 (1998).
- 9 4. Salomatina, E. V., Jiang, B., Novak, J. & Yaroslavsky, A. N. Optical properties of normal and
10 cancerous human skin in the visible and near-infrared spectral range. *J Biomed Opt* **11**, 064026
11 (2006).
- 12 5. Roggan, A., Dörschel, K., Minet, O., Wolff, D. & Müller, G. The optical properties of biological
13 tissue in the near infrared wavelength range: review and measurements. *SPIE Optical
14 Engineering Press* 10–44 (1995).